Compensated Ferrimagnets For Spintronic Applications

A Thesis

submitted to
Indian Institute of Science Education and Research Pune
in partial fulfillment of the requirements for the
BS-MS Dual Degree Programme

by

P B S Murthykrishnan

Indian Institute of Science Education and Research Pune
Dr. Homi Bhabha Road
Pashan, Pune 411008, INDIA.

Decemeber, 2021

Supervisor: Dr. Sunil Nair

Certificate

This is to certify that this dissertation entitled **Compensated Ferrimagnets for Spintronic Applications** towards the partial fulfilment of the BS-MS dual degree programme at the Indian Institute of Science Education and Research, Pune represents study/work carried out by P B S Murthykrishnan at Indian Institute of Science Education and Research under the supervision of Dr. Sunil Nair, Associate Professor, Department of Physics , during the academic year 2020-2021.

Dr. Sunil Nair

Committee: Physics

Dr. Sunil Nair

Dr. Mukul Kabir

This thesis is dedicated to Jo

Declaration

I hereby declare that the matter embodied in the report entitled Compensated Ferrimagnets for Spintronic Applications is result of the work carried out by me at the Department of Physics, Indian Institute of Science Education and Research, Pune, under the supervision of Dr. Sunil Nair and the same has not been submitted elsewhere for any other degree.

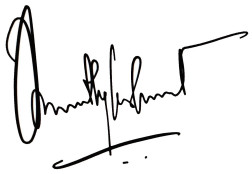

P B S Murthykrishnan

Acknowledgements

I would firstly like to thank my supervisor, Dr. Sunil Nair for his continuous guidance and motivation through out the course of the project. His unwavering faith in me even in the light of my various frailties gave me tremendous self belief and drive to keep working towards the progress of my project. I'm deeply indebted towards him on both a personal and professional level.

Next I would like to thank all my lab mates for their encouragement and support in the form of various discussions we have had which I believe helped to expand my overall aptitude and knowledge of the field. At this juncture I would like to extend my sincere gratitude to my PhD guide and friend Anna Merin Francis who was with me through thick and thin and provided the perfect environment for me to work as efficiently as possible, being a pillar of support during my times of need. It is safe to say that I would not have been able to do this without her and I thoroughly enjoyed my time working with her. Special thanks also to Dr. Avirup Dey, for allowing me to use the spin Seebeck measurement setup that he had built.

I would also like to thank Swati for her help in thin film fabrication, her expertise in the field was a valuable asset to have. I would also like thank Mr. Sudheer whose help was invaluable in operating the magnetron sputtering and FESEM facilities. I must also thank Irfan and Umashankar for helping me with the AFM measurements.

Furthermore I'm grateful to my TAC, Dr. Mukul Kabir for his valuable insights and probing questions which challenged and helped to further my understanding of the topic.

Finally I would like thank my family for their constant care and support throughout my life for which I'm deeply grateful. I would like to especially thank my brother for bringing joy to my life. All of this would not have been possible without them.

Abstract

Antiferromagnetic spintronics is increasingly in vogue owing to advantages like the relative insensitivity of these systems to external magnetic fields, and the ultrafast nature of their spin dynamics which can have a number of potential uses. In this context, compensated ferrimagnets are also attracting increasing attention, due to the fact that they combine some of the advantages of both the ferro and antiferro- magnetically ordered systems. Intrinsically antiferromagnetic with two uncompensated sub-lattices, the bulk magnetization of such systems can be tuned to zero using number of external parameters like chemical substitution, strain, temperature etc.

In this project, we investigated some garnet compositions (ferrites of the form $A_3Fe_3O_{12}$, where A is a rare earth), namely Gadolinium Iron Garnet($Gd_3Fe_5O_{12}$), Yttrium Iron Garnet($Y_3Fe_5O_{12}$) and Ytterbium Iron Garnet($Yb_3Fe_5O_{12}$) with the aim of evaluating their potential as spintronic materials. The different garnet compositions were synthesised via the solid state route, with the aim of tuning the compensation temperature to be very close to room temperatures, this was achieved by doping $Gd_3Fe_5O_{12}$ with "Mn" of different concentrations on the octahedral "Fe" site. The temperature and field dependent spin transport in these bulk systems were investigated using Spin Seebeck measurements.

Contents

1 Introduction **12**
- 1.1 Why Spintronics ? . . . 12
  - 1.1.1 What is a spin current ? . . . 13
- 1.2 Spin Hall Effect . . . 15
- 1.3 Spin Seebeck Effect . . . 16
- 1.4 Compensated Ferrimagnets . . . 19
  - 1.4.1 Iron Garnets . . . 19
- 1.5 Aim of the Thesis . . . 20

2 Experimental Methods **22**
- 2.1 Synthesis . . . 22
  - 2.1.1 Synthesis of Gadolinium Iron Garnet . . . 22
  - 2.1.2 Synthesis of Yttrium Iron Garnet . . . 23
  - 2.1.3 Synthesis of Ytterbium Iron Garnet . . . 23
  - 2.1.4 Synthesis of Mn doped GdIG . . . 24
- 2.2 X-Ray Diffraction (XRD) . . . 24
- 2.3 Structural Analysis . . . 25
- 2.4 Field Emission Scanning Electron Microscopy and Energy Dispersive X-Ray Spectroscopy . . . 27
- 2.5 Sputtering . . . 28
- 2.6 Atomic Force Microscopy (AFM) . . . 30
- 2.7 Spin Seebeck Measurement Unit . . . 31

3 Results And Discussion **33**
- 3.1 Structural Analysis . . . 33
  - 3.1.1 Gadolinium Iron Garnet(GdIG) - $Gd_3Fe_5O_{12}$ . . . 33
  - 3.1.2 $Gd_3Fe_{4.96}Mn_{0.04}O_{12}$ (GdMnIG 4% Mn doped) . . . 36
  - 3.1.3 $Gd_3Fe_{4.92}Mn_{0.08}O_{12}$ (GdMnIG 8% Mn doped) . . . 38
  - 3.1.4 $Gd_3Fe_{4.9}Mn_{0.1}O_{12}$ (GdMnIG 10% Mn doped) . . . 41
  - 3.1.5 Ytterbium Iron Garnet - $Yb_3Fe_5O_{12}$ . . . 42
  - 3.1.6 Yttrium Iron Garnet(YIG) - $Y_3Fe_5O_{12}$ . . . 44
- 3.2 Spin Seebeck Measurements . . . 45
  - 3.2.1 GdIG . . . 45
  - 3.2.2 GdMnIG 4% Mn Doped . . . 48

3.2.3 GdMnIG 8% Mn Doped 51
3.2.4 $Yb_3Fe_5O_{12}$ - YbIG 53

4 Conclusions And Future Work **55**

List of Figures

1.1 Working of principle GMR and TMR devices[5] 13
1.2 Illustration of relationship between heat and spin current.[6] 13
1.3 Different types of conduction electron currents[10] 14
1.4 Spin current due to spin wave[12] 15
1.5 (a)Spin Hall effect (b) Inverse spin Hall effect[18] 16
1.6 (a)Illustrates the concept of the spin Seebeck effect (b) From this figure, we can see how the ANE could affect the strength of the spin Seebeck signal in the longitudinal arrangement (c)and(d) Representation of the Longitudinal spin Seebeck effect and the ISHE which is used to convert the spin current into a detectable charge current.[28] 18
1.7 (a) Shows the magnetic sublattice of GdIG (b) and (c) Illustrates the temperature dependence of the magnetic sub layers in GdIG[35] . . . 20

2.1 Figure illustrates the reflection of X-rays by lattice planes separated by distance 'd'. The scattered X-rays only interfere constructively if they satisfy the Bragg's condition given above.[46] 25
2.2 Figure shows a schematic of FESEM[51] 28
2.3 Figure shows a schematic of the working of a DC Magnetron sputtering system[53] 29
2.4 (a) Shows Pt bar coated on top of GdIG slab. (b)Here two gold wires are attached to the ends of the Pt bar using Silver paste and a sapphire plate is cut such that it just covers the Pt bar in between the contacts. This sapphire plate is placed on top of the slab using Apiezon grease. . 30
2.5 AFM image obtained for GdIG shows thickness of Pt layer deposited is roughly 20nm 31
2.6 (a) Shows the sample holder onto which the prepared slab is loaded. (b)The SSE measurement set up is placed inside a Faraday cage in order to minimize noise. 32

3.1 FESEM images showing micron sized crystallites of GdIG 33
3.2 Rietveld plot for $Gd_3Fe_5O_{12}$ 34
3.3 Shows the XRD data obtained for GdIG and GdMnIG(4%). Here we can see extra peaks after the 10hr heat treatment indicating that the pure phase has not formed but these were removed upon a further 24hr heat treatment 36

3.4 Rietveld refinement fit for $Gd_3Fe_{4.96}Mn_{0.04}O_{12}$ 38
3.5 On comparing the XRD data of GdMnIG(8%) with that of GdIG we can see that there is a small extra peak which was suspected to be that of alumina. 39
3.6 Rietveld fitting profile of $Gd_3Fe_{4.92}Mn_{0.08}O_{12}$. 41
3.7 XRD data of $Gd_3Fe_{4.9}Mn_{0.1}O_{12}$ shows a very major impurity peak of alumina, with a relative intensity of almost 30 percent with respect to the largest parent peak. 42
3.8 Rietveld refinement fit for $Yb_3Fe_5O_{12}$ 43
3.9 Rietveld refinement fit for $Y_3Fe_5O_{12}$ 44
3.10 Figure shows the zero field temperature dependent resistance measurements done on GdIG/Pt slab. The resistance shows a linear trend with y-intercept = 861.669 ± 0.221 and slope 0.9427 ± 0.0012 46
3.11 Figure shows temperature dependence of the SSE signal with temperature. Here we can clearly see the two transition points where the sign of the signal has flipped. Other than the two transition points we can see that signal value peaks at around 200K, this peak in intensity can be attributed to the magnon population and magnon lifetimes. 47
3.12 Figure shows the hysteresis of the spin Seebeck signal of $Gd_3Fe_5O_{12}$ measured at 200K with a ΔT of 20K. The signal saturates at around 1500 Oe. The fact that the loop doesn't exactly close can be attributed to a shift in the background. 48
3.13 Figure shows the hysteresis of the spin Seebeck signal of $Gd_3Fe_5O_{12}$ measured at 300K with ΔT of 20K.Here the overall signal strength is considerably less than that at 200K and polarity of the signal is also flipped, this can be explained on the basis of the reversal of the sublattice magnetisation at T_{comp}. 48
3.14 Figure shows the zero field temperature dependent resistance measurements done on GdIG/Pt slab. The resistance shows a linear trend with y-intercept = 252.1303 ± 0.1489 and slope 0.4141 ± 0.0008 49
3.15 We can clearly see the two transitions points and also to be noted is that the signal strength peaks at around 210K which is around a +10K shift from what was observed in GdIG 50
3.16 Figure shows the hysteresis of the spin Seebeck signal at 200K with a ΔT = 20K. The polarity of the signal is same as the one obtained for GdIG in the temperature regime where $T < T_{comp}$ 50
3.17 (a)Shows the zero field temperature dependent resistance measurements done on GdIG/Pt slab. The resistance shows a linear trend with y-intercept = 109.6327 ± 0.0624 and slope 0.1827 ± 0.0003. (b)There are two transition points like in the case of both GdIG and GdMnIG 4% doped samples. There is no real change in the second transition point as compared to the previous samples but there is a 5K decrease in the transition point from GdMnIG 4% 51
3.18 (a) and (b) Shows hysteresis of SSE signal at 200K and 300K respectively. The polarity of the signal is flipped due to spin reorientation at the compensation point. 52

3.19 (a) Compares SSE signal strength of GdIG and 4% Mn doped GdMnIG and (b) Compares the SSE signal strength of GdIG, 4% Mn doped and 8% Mn doped GdMnIG. From (a) and (b) it can be clearly seen that with 8% Mn doping the signal strength is almost an order of magnitude greater than the other two. 53
3.20 Figure shows the zero field temperature dependent resistance measurements done on YbIG/Pt device. The resistance shows a linear trend with y-intercept = 681.5407 ± 0.5326 and slope 1.2128 ± 0.0029 . . . 54
3.21 Figure shows the spin Seebeck voltage as a function of temperature . 54

List of Tables

2.1 Reaction protocol for $Gd_3Fe_5O_{12}$ 23
2.2 Reaction protocol for $Y_3Fe_5O_{12}$ trial 23
2.3 Reaction protocol for $Y_3Fe_5O_{12}$ Bulk 23
2.4 Reaction protocol for $Yb_3Fe_5O_{12}$ trial 24
2.5 Reaction protocol for $Gd_3Fe_{5-x}Mn_xO_{12}$(x =0.04, 0.08, 0.1) trials . . . 24

3.1 Lattice and fitting parameters of $Gd_3Fe_5O_{12}$ obtained from Rietveld refinement 35
3.2 Refined atomic positions and fractional occupancy 35
3.3 Lattice and fitting parameters of $Gd_3Fe_{4.96}Mn_{0.04}O_{12}$ obtained from Rietveld refinement 37
3.4 Refined atomic positions and fractional occupancy 37
3.5 Lattice and fitting parameters of $Gd_3Fe_{4.92}Mn_{0.08}O_{12}$ obtained from Rietveld refinement. Comparing the unit cell parameters of $Gd_3Fe_5O_12$ with that of $Gd_3Fe_{4.96}Mn_{0.04}O_{12}$ and $Gd_3Fe_{4.92}Mn_{0.08}O_{12}$ we can see a decrease in the unit cell parameter magnitudes with increasing concentrations of Mn doping. 40
3.6 Refined atomic positions and fractional occupancy. Here the occupancies of Mn1, Mn2, Fe1, and Fe2 are not exactly consistent with the theoretical predictions. This may be attributed to the presence of the alumina in the sample which maybe influencing the refinement 41
3.7 Lattice and fitting parameters of $Yb_3Fe_5O_{12}$ obtained from Rietveld refinement. 43
3.8 Refined atomic positions and fractional occupancy of YbIG 44
3.9 Lattice and fitting parameters of $Y_3Fe_5O_{12}$ obtained from Rietveld refinement. 45
3.10 Refined atomic positions and fractional occupancy of YIG 45

Chapter 1

Introduction

1.1 Why Spintronics ?

Electronic based devices have been around for more than half a century. Advancements in computing power have so far relied on packing more and more devices into smaller and smaller spaces, thereby increasing the density, but physical limitations will eventually bring an end to further developments along this route. Furthermore, most of today's electronics industry is based on volatile memory, which hinders faster processing times. However, "Spintronics" is an emerging field that has the potential to change all that, where both charge and spin degrees of freedom of electrons are used for the transport and storage of information.[1]

The field of spintronics was, for all practical purposes, kick-started by the discovery of an effect called Giant magnetoresistance(GMR), which in turn led to the development of the "Spin valve" [2][3]which forms the core of most modern-day memory devices. GMR refers to an effect observed in multi-layers of alternating ferromagnetic and non-magnetic conducting layers. The effect is observed as a significant drop (or increase) in the electrical resistance depending on the magnetisation of the adjacent ferromagnetic layers. If the magnetisation of the layers is parallel, then the resistance is low, and if the orientation is antiparallel, then the resistance is high. This phenomenon is explained based on spin-dependent scattering, where scattering depends on the relative orientations of the electron spins and those magnetic moments: it is weakest when they are parallel and strongest when they are antiparallel.[4]

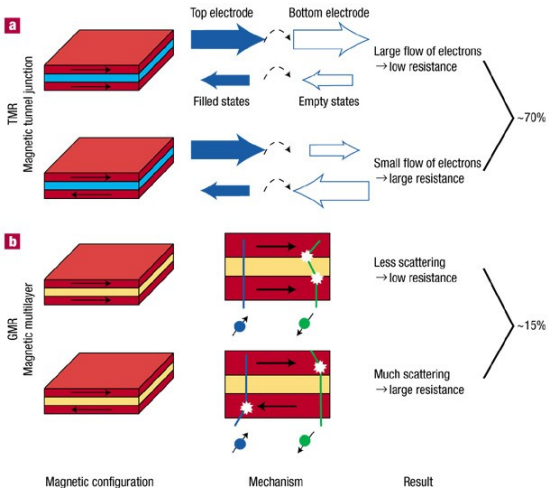

Figure 1.1: Working of principle GMR and TMR devices[5]

Furthermore, the discovery of Tunnel magnetoresistance, where a thin insulating layer replaces the nonconducting magnetic layer in the GMR, which allows for greater magnetoresistance, has revolutionised modern-day solid-state technology.

Apart from coupling the charge and spin degrees of freedom on electrons, the utilisation of pure spin current has been of substantial interest in recent times, where the focus has been on understanding the generation, detection and characterisation of such spin current in materials. Along this avenue, there has been particular interest in the interactions between spin and heat currents, giving birth to a sub field of spintronics called ”Spin-caloritronics”.

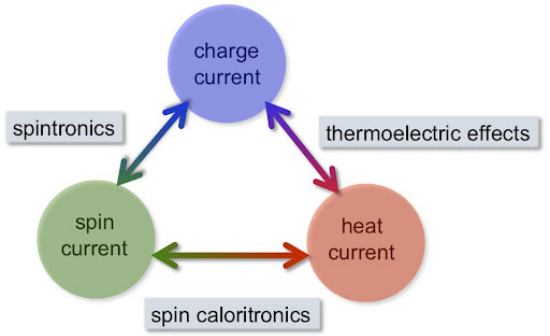

Figure 1.2: Illustration of relationship between heat and spin current.[6]

1.1.1 What is a spin current ?

Spin currents are at the heart of all spintronics; hence knowledge of spin currents is indispensable for understanding the field of spintronics. By definition, a spin current is

described as a flow of angular momentum. A spin current J_s is given by :

$$J_s = \sum_k s_k^z v_k$$

where s_k^z is z-component of the spin current density s_k with the z-axis chosen as the axis of quantisation and $v_k$is the velocity of the excitation associated with the spin density s_k.[7] In materials, we can describe two different types of spin currents. One is because of the conduction electrons, whose spin angular momentum contributes to the spin current via the spin-dependent flow of electrons. The other type is called the magnon spin current, where magnons are the quasi-particles associated with spin excitation.[8] Along with spin currents, another essential concept to be understood would be that of pure spin-current[9]. A pure spin current is one which does not have any associated charge current. Therefore it can be seen that in the case of conduction electron spin current we require the flow of oppositely oriented spins in equal and opposite direction so that there is a net spin potential that is developed but there is no net charge current. And in this case the spin density can be given by

$$s_z^k = d_{k,\uparrow}^\dagger d_{k,\uparrow} - d_{k,\downarrow}^\dagger d_{k,\downarrow}$$

, where $d_{k,\uparrow}^\dagger$ and $d_{k,\downarrow}^\dagger$are the creation operators for conduction electrons with momentum k. After taking a statistical average the conduction-electron pure spin current J_s^{el} can be written as

$$J_s^{el} = \sum_k v_k \left(\langle d_{k,\uparrow}^\dagger d_{k,\uparrow} \rangle - \langle d_{k,\downarrow}^\dagger d_{k,\downarrow} \rangle \right)$$

.

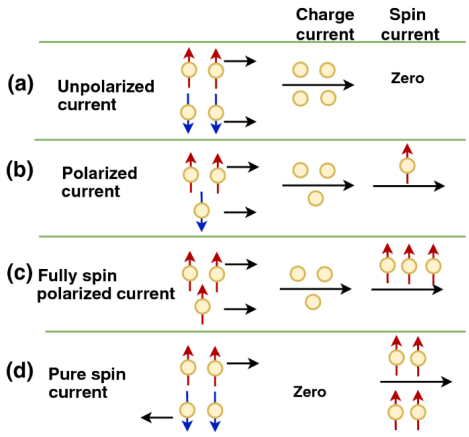

Figure 1.3: Different types of conduction electron currents[10]

In similar fashion we can also describe a pure magnon spin-current, where the z-component of the spin density is given by

$$s_k^z = S_0 - m_k^\dagger m_k$$

, where $m_k^\dagger$ is the creation operator of magnons with momentum k. As was the case with the conduction electrons we take a statistical average, then the expectation value of the magnon pure spin current is given by

$$J_s^{mag} = -\frac{1}{2}\sum_k v_k \left(\langle m_k^\dagger m_k \rangle - \langle m_{-k}^\dagger m_{-k}, \rangle \right)$$

, where v_K is the magnon velocity and v_{-k}=$-v_k$[8][11]

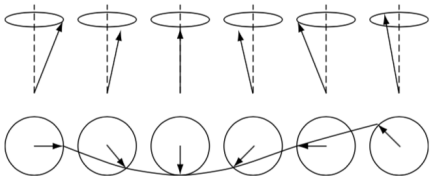

Figure 1.4: Spin current due to spin wave[12]

A critical distinction between the two types of spin currents is that the spin diffusion length of the conduction electron spin current is very small(of the order of a few nanometers), limiting the spin current's propagation length. However, in the case of the magnon spin current, the propagation length has been observed to be over a macroscopic scale of around a millimeter[13]. Another advantage of magnon spin current is that there is no associated charge current, avoiding Joule heating.

Now that we know what a spin current is, the next step will be to understand the inter-conversion between charge and spin currents. Moreover, the electrical generation of spin current is at the heart of spintronics.

1.2 Spin Hall Effect

The phenomenon known as Spin-Orbit coupling allows for charge currents to be converted into spin currents and vice versa[7]. Among the various ways to produce and control these spin currents, the Spin-Hall effect(SHE)[14] has shot to prominence over the last decade and is one of the most widely used methods to generate spin currents.

The Spin-Hall effect, first predicted by Mikhail I. Dyakonov and Vladimir I. Perel in 1971 refers to the generation of a non-zero spin current [15]in the direction perpendicular to the applied charge current[16]. There two principles that are commonly used in describing the origin of SHE. the first one is an extrinsic approach using spin dependent Mott-scattering where carriers of opposite spins deflect along opposite directions. The second is due to intrinsic characteristics of any material and has to do with spin-orbit interactions[17]. Due to spin-orbit interactions the scattered electrons attain a spin polarisation[8], given by

$$\widehat{\sigma} \propto \widehat{k_{in}} \times \widehat{k_{out}},$$

where $\widehat{k_{in}}$ and $\widehat{k_{out}}$ are the incident and scattered wave vectors respectively. Macroscopically the spin Hall effect can be expressed as

$$\tilde{J}_s = \theta_H \widehat{\sigma} \times J_c,$$

where θ_H, $\widehat{sigma}$, $\tilde{J}_s$ and J_c are the spin-Hall angle, spin polarization vector, spin current and charge current respectively.

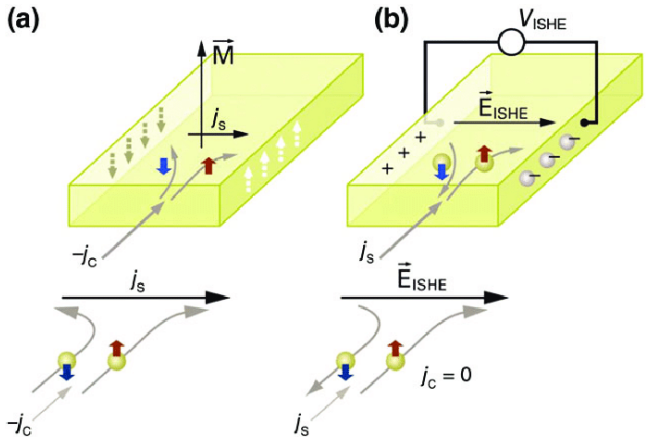

Figure 1.5: (a)Spin Hall effect (b) Inverse spin Hall effect[18]

As we have discussed a mechanism to generate spin currents, we need mechanisms to detect it. Furthermore, here is where the concept of Inverse spin-Hall effect(ISHE)[19][7] comes in. It is a process by which a spin current injected into a metal with a large spin-orbit coupling generates a charge current perpendicular to both the spin polarization and the spin current. Similar to the SHE, the ISHE can be written down as

$$J_c = \theta_H \widehat{\sigma} \times \tilde{J}_s,$$

where we can write $\tilde{J}_s = J_c$ We require large spin-orbit coupling for a more significant signal; non-magnetic metals like Pt, W or Ta are generally used for detection purposes.

So far, we have discussed the spin currents without really talking about the involvement of heat. But as mentioned previously, the interplay between this spin current and heat gives rise to a whole host of exciting and new phenomena, and these are what we will be primarily focused on in this thesis, chief of which is the spin-Seebeck effect.

1.3 Spin Seebeck Effect

The spin-Seebeck effect refers to the generation of a spin voltage upon the application of a thermal gradient in a ferromagnet[20]. This effect can drive a spin current into a non-magnetic layer from a Tferromagnetic layer over a macroscopic scale of several millimetres, where it is converted back into an inverse charge voltage by the ISHE[21].

The spin-Seebeck effect(SSE) has been reported in two configurations, the "Transverse" SSE and "Longitudinal" SSE. The "Transverse" SSE refers to a spin current generated perpendicular to the temperature gradient applied. It was first observed in $Ni_{81}Fe_{19}$ films and was later used in SSE measurements in insulators and semiconductors[22][23]. However, when conductive ferromagnets were used, the SSE signals were contaminated by the Anomalous Nernst Effect(ANE)[24]. ANE is when a charge current is produced perpendicular to both an applied temperature gradient ΔT and magnetic field. The second configuration is the "Longitudinal" one, which was first demonstrated in $Pt/Y_3Fe_5O_{12}$ (YIG) systems in 2010 [25][26]. The basic setup involves a paramagnetic metal film that is deposited on top of a ferromagnetic insulator. A temperature gradient is applied perpendicular to the ferromagnetic layer, and a spin voltage is generated, and a spin current is pumped into the non-magnetic layer. The spin current is then converted into an electric field[27], E_{ISHE}[28] via the ISHE.

$$E_{ISHE} \propto J_s \times \sigma$$

, where J_s is the spatial direction of the spin current-induced and σ is spin polarisation on the electrons.[29]

It has been shown that the conduction electrons alone cannot explain the spin-Seebeck effect because the spin diffusion length of the conduction electrons is only of the order of a few nanometers, which is at odds with the long-range(millimetres) readings observed in experiments. This is further supported by the fact that SSE was observed in ferromagnetic insulator YIG[30]. Hence it was concluded that magnons carried the spin current. So now it is believed that SSE is caused due to a non-equilibrium between the magnons in ferromagnet[31] and the conduction electrons in the non-magnetic layer.[8]

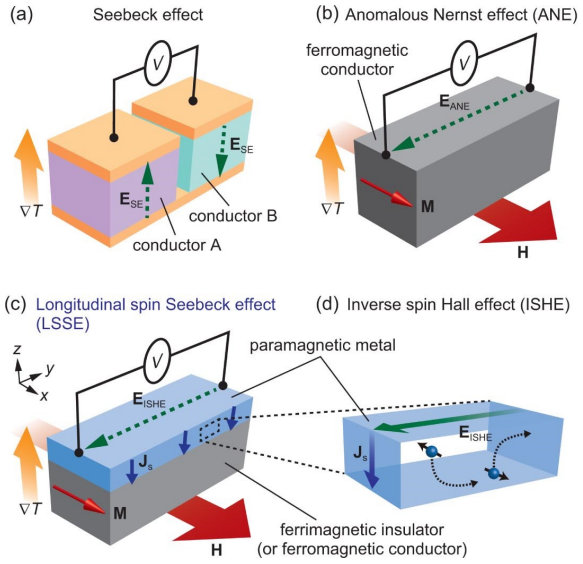

centring

Figure 1.6: (a)Illustrates the concept of the spin Seebeck effect (b) From this figure, we can see how the ANE could affect the strength of the spin Seebeck signal in the longitudinal arrangement (c)and(d) Representation of the Longitudinal spin Seebeck effect and the ISHE which is used to convert the spin current into a detectable charge current.[28]

The amount of spin current that is pumped into the non magnetic detection layer depends on the interfacial spin pumping. Here spin pumping[32][22] depends on the interaction between the conduction electrons and localised spins at the interface of the magnetic and non magnetic layer. This is quantified by a parameter called the spin mixing conductance given by $g_{\uparrow\downarrow}$. And the amount of spin current pumped is mathematically related to the thermally activated magnetisation dynamics at the interface, and the magnetisation dynamics is modelled upon the Landau-Lifshitz-Gilbert (LLG) equation give by

$$\frac{\partial M}{\partial t} = \left[\gamma(H_0 + h) - \frac{J_{sd}}{\hbar} s\right] \times M + \frac{\alpha}{M_s} M \times \frac{\partial M}{\partial t}$$

, where $H_0 = H_0\hat{z}$ is the external field, γ is the gyromagnetic ratio, α is the Gilbert damping constant[33] and M_s is the saturation magnetization and h represents the thermal fluctuations in the ferromagnetic layer.

Now that we have got to grips with the underlying mechanisms at play in the field of spin caloritronics, we would next require a system to test these on. We have mentioned above that in the case of SSE, the configuration that has become the industry standard is the Longitudinal one, and for that, it is best to use a system with an insulating magnetic layer on top of which we would deposit a non-magnetic layer, usually a "Normal metal"(NM) with high spin-orbit coupling like Pt, Ta or W. Here a prevalent system of magnetic insulators used are known as "Compensated Ferrimagnets".

1.4 Compensated Ferrimagnets

A ferrimagnetic material has populations of opposing magnetic moments similar to what is found in antiferromagnets, but unlike antiferromagnets, the magnitude of these moments is not equal, leading to spontaneous magnetisation. These different magnetic moments can be viewed in terms of magnetic sublattices of opposing magnetisation, where the magnitude of one is greater than that of the other. Now the molecular field on each sublattice is different; hence the spontaneous magnetisation of the sublattices will, in general, have different temperature dependencies, leading to the net magnetisation of the material to have a rather complicated temperature dependence [34]. It has been observed in some cases that the magnetisation of one sublattice dominates at lower temperatures where as the other one dominates at higher temperatures, this, in turn, leads to the possibility of reducing the net magnetisation to zero and change sign at a temperature known as the compensation temperature[35]. Therefore, this state is known as the compensated state, and such ferrimagnets are known as "Compensated ferrimagnets". Furthermore, this compensation state can be achieved by tuning specific parameters like chemical composition and strain.

Among the many categories of ferrimagnets, three have been of particular interest in the context of spintronics. The first is the rare-earth (RE) transition metal (TM) alloy. RE-TM alloys consist of RE (Gd, Yb, Tb, etc.) and TM (Fe, Ni, etc.), and the magnetic moment of these alloys are based on the electrons in the f and d orbitals, respectively. And exchange interactions between these d and f electrons can lead to anti-ferromagnetic coupling. Another point of interest with RE-TM alloys is that the magnetisation at a given temperature depends on the relative concentrations of each element, leading to a highly tunable system. [36]

Apart from RE-TM, some Heusler alloys also exhibit tunable ferrimagnetism[37]. Heusler compounds are a class of intermetallics with up to four elements. They exhibit face-centred cubic crystal structure and compositions of XYZ (half-Heuslers) and X_2YZ (full-Heuslers) where X and Y are transition metals, and Z is either semiconductor or normal metals. Due to many different elements, it is possible to engineer many properties like magnetic order, multiferroicity, etc.

Other than RE-TM alloys and Heusler compounds, Garnets are another class of compounds that have been extensively investigated. Garnets have exhibited compensation temperatures close to room temperature, have ultra-fast domain wall motion and are switchable via spin-orbit torque[38]. Garnets being insulators also can have extensive application in spintronics as they improve efficiency by eliminating Joule heating. This insulating nature is very attractive in spin caloritronics as it helps in studying the spin Seebeck effect and is also the primary system that we will be investigating in this thesis.

1.4.1 Iron Garnets

Garnets are insulators with desirable magnetic properties such as high Curie temperature, highly tunable bulk perpendicular magnetic anisotropy (PMA), ferrimagnetic nature with a low net moment, extremely low Gilbert damping, etc. making them particularly suitable for applications in the next generation spintronic devices[39], which

exhibit low energy consumption, room temperature fast operation speed and high integration density[40]. Iron garnets have the form $A_3Fe_5O_{12}$, where A is a rare earth element, and they crystallise in the $Ia3d$ space group. Here the rare earth element is present in the +3 oxidation state, and the iron atoms also have an oxidation state of +3. Each unit cell consists of 12 trivalent Fe atoms that are tetrahedrally coordinated with oxygen atoms (d-site), 8 Fe atoms that are octahedrally coordinated (a-site) and 12 dodecahedrally coordinated "A" atoms (c-site). The magnetism is carried by localised Fe moments in 8 tetrahedral (minority) and 12 octahedral (majority) oxygen cages per unit cell, with an anti-parallel ferrimagnetic state between the two coordinations.

This thesis looks explicitly at the garnet, Gadolinium iron garnet (GdIG). This is due to the fact that GdIG is reported to have a compensation temperature of around 288K, which is the highest among all the rare earth iron garnets. From the above discussion, we can see that the Fe *a* sublattice and Fe *d* sublattice are coupled by antiferromagnetic super-exchange, and since Gd is weakly exchange coupled with the Fe *a* site sublattice, they experience an effective magnetic field below the Neel temperature, T_N and can be treated as an 'exchange enhanced' paramagnetic moment, which is strongly temperature dependent.[35]

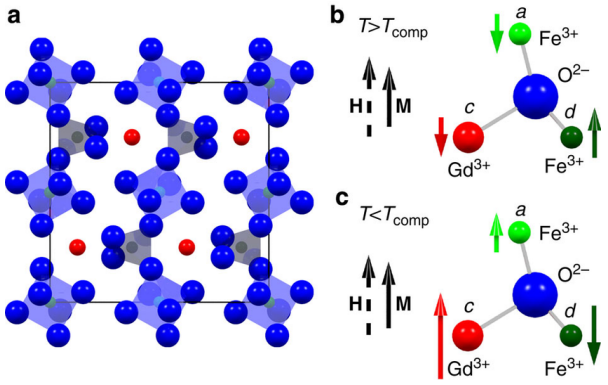

Figure 1.7: (a) Shows the magnetic sublattice of GdIG (b) and (c) Illustrates the temperature dependence of the magnetic sub layers in GdIG[35]

Hence at high temperatures, the magnetisation of GdIG is determined by the *d* site Fe sublattice. But as the temperature decreases, the magnetic moment of the Gd sublattice strongly increases and, together with the magnetisation of the *a* site Fe sublattice, will eventually cancel out the magnetic moment of the *d* site Fe sublattice and overcome it as we continue of further decrease the temperature.

1.5 Aim of the Thesis

In this thesis, our primary goal will be to tune the compensation temperature of GdIG. This can be achieved, as mentioned previously, by changing the composition of the material via doping. Here we will be doping GdIG with Mn where Mn is being doped

on the d-site Fe because, as shown above, the net magnetisation depends on the sum of magnetisation of Gd and Fe(a-site) versus the Fe(d-site) magnetisation. So the idea is that if we can replace the d-site Fe with an element of lower magnetic moment, we would be able to reduce the effective magnetic moment of the d-site and hence push the compensation temperature more towards room temperature. Moreover, if we can sufficiently change the compensation point, we could utilise this property in the fabrication of prototypical spin controlled devices. In addition to this, we would also try to synthesis garnets other than GdIG, namely Ytterbium Iron Garnet(YbIG) and Yttrium Iron Garnet(YIG). The synthesised samples will be characterised and studied with the help of spin Seebeck measurements.

Chapter 2

Experimental Methods

2.1 Synthesis

All compounds were prepared via solid state synthesis. The appropriate raw materials were taken keeping in mind the stoichiometry of the end product. Also the reactants were chosen to be in powdered form as this would increase the surface area and thereby increase the reactivity. After weighing, the raw materials are mixed thoroughly via agate mortar and pestle. Special care was given while mixing such that the mixture was homogeneous. In order to aid in the formation of a homogeneous mixture some amount of volatile organic liquid - in this case 99.99 percent ethanol was used during the mixing process. Once the mixture has been adequately homogenized, the mixture was pressed into pellets with the help of a KBr press, Pelletization is done in order to increase the area of contact between the grains[41]. Since solid state reactions are intrinsically slow, a high temperature environment is necessary. Hence the reactions were done at temperatures between 1200^oC and 1400^oC. All reactions except for reactions involving *Mn* doped *GdIG* were done using alumina crucibles. In the case of *Mn* doped *GdIG* a Platinum crucible was used. The high temperatures required for the reaction was achieved by using PID controlled programmable furnaces. The product samples once formed were subjected to Powder X-Ray Diffraction(PXRD) and Energy Dispersive X-Ray Spectroscopy.

2.1.1 Synthesis of Gadolinium Iron Garnet

Synthesis of Gadolinium Iron Garnet(GdIG) was done via solid state synthesis[42]. Stoichiometric amounts of Fe_2O_3(99.9%) and Gd_2O_3(99.99%) were weighed and mixed together in a pestle and mortar using 99.99 percent ethanol. Initially a 1gm trial sample was prepared and consequently a 5gm bulk amount was prepared. The reaction was carried out in P310 Nabertherm furnace in air atmosphere at 1200^oC for 10 hours. A differential heating rate was applied in order to inhibit the formation of the perovskite phase $GdFeO_3$ which stabilizes around 800 to 1000^oC. The balanced equation is given below[43]:

$$5Fe_2O_3 + 3Gd_2O_3 \rightarrow 2Gd_3Fe_5O_{12}$$

Compound	Temp (^{o}**c**)/Time	Environment and rate
GdIG	1200 ^{o}**c**/10hr	air, 4 $^o c$/min upto 650 $^o c$ and 10 $^o c$/min from 650 to 1200 $^o c$

Table 2.1: Reaction protocol for $Gd_3Fe_5O_{12}$

2.1.2 Synthesis of Yttrium Iron Garnet

The raw materials in this case were Y_2O_3(99.99%) and Fe_2O_3(99.9%), these were weighed out according to the stoichiometry of the reaction and mixed together using mortar and pestle using 99.9% ethanol. Initially a 1gm trial sample was prepared, then a 5gm bulk sample was prepared. The reaction protocol for trial and bulk samples were different. In the case of the trial, three different heat treatments were required, were the same differential heating rate used in the GdIG was used to curb the formation of the $YFeO_3$ perovskite phase. As for the bulk samples a different protocol was used as a pure phase was not being obtained with protocol used for the trial, the reaction protocols for both the bulk and trial samples are given in Table 1.2 . The reaction was carried out according to the equation given below[44] :

$$5Fe_2O_3 + 3Y_2O_3 \rightarrow 2Y_3Fe_5O_{12}$$

.

Treatments	Temp(^{o}**c**)/Time	Environment and rate
T1	1200^o**c**/10hr	air,4 $^o c$/min upto 650 $^o c$ and 10 $^o c$/min from 650 to 1200 $^o c$
T2	1200^o**c**/24hr	
T3	1200^o**c**/10hr	O_2, same rate as above

Table 2.2: Reaction protocol for $Y_3Fe_5O_{12}$ trial

Compound	Temp(^{o}**c**)/Time	Environment and rate
YIG Bulk	1400^o**c**/6hr	air, 4 $^o c$/min upto 650 $^o c$ and 10 $^o c$/min from 650 to 1400 $^o c$

Table 2.3: Reaction protocol for $Y_3Fe_5O_{12}$ Bulk

2.1.3 Synthesis of Ytterbium Iron Garnet

Ytterbium Iron Garnet (YbIG) was synthesised with Yb_2O_3(99.99%) and Fe_2O_3(99.9%). The raw materials were weighed out stoichiometrically and ground together with mor-

tar and pestle with the help of 99.99% ethanol. The reaction protocol is given in Table 1.4. A differential heating rate was employed in this case as well in order to inhibit formation of $YbFeO_3$ perovskite phase. The reaction was carried out based on the following reaction:

$$5Fe_2O_3 + 3Yb_2O_3 \rightarrow 2Yb_3Fe_5O_{12}$$

.

Treatments	Temp(^{o}**c**)/Time	Environment and rate
T1	1200^o**c**/10hr	air,4 $^o c$/min upto 650 $^o c$ and 10 $^o c$/min
T2	1200^o**c**/24hr	from 650 to 1200 $^o c$
T3	1200^o**c**/10hr	O_2, same rate as above

Table 2.4: Reaction protocol for $Yb_3Fe_5O_{12}$ trial

2.1.4 Synthesis of Mn doped GdIG

A total of 3 trials of Mn doped GdIG (GdMnIG) were synthesised where the concentration of Mn dpoing was varied. The trials include a 4%, 8% and 10% Mn doped GdIG. Here GdMnIG can be written as $Gd_3Fe_{5-x}Mn_xO_{12}$(x = 0.04, 0.08, 0.1). The raw materials used were Fe_2O_3(99.9%), Gd_2O_3(99.99%) and Mn_2O_3(99.99%). These were weighed in appropriate amounts and ground into a homogenized mixture. The reaction for all the different trials of GdMnIG were done in O_2 atmosphere, the reaction is given as follows:

$$(5-x)Fe_2O_3 + 3Gd_2O_3 + xMn_2O_3 \rightarrow 2Gd_3Fe_{5-x}Mn_xO_{12}$$

. The x =0.04 and x =0.08 required 2 separate heat treatments, whereas for x =0.1 only one heat treatment was required. Reaction protocol followed for the different trails are given in table 1.5.

Mn concentration	Temp(^{o}**c**)/Time	Rate
x =0.04	1200^o**c**/10hr and 1200^o**c**/24hr	4 $^o c$/min upto 650 $^o c$ and 10 $^o c$/min from 650 to 1200 $^o c$
x =0.08	1200^o**c**/10hr and 1200^o**c**/24hr	
x =0.1	1200^o**c**/10hr	

Table 2.5: Reaction protocol for $Gd_3Fe_{5-x}Mn_xO_{12}$(x =0.04, 0.08, 0.1) trials

2.2 X-Ray Diffraction (XRD)

X-Ray diffraction techniques were used in order to confirm the formation of pure phase. XRD is a powerful and versatile tool that gives us information regarding the chemical composition and crystallographic structure of materials. When X-rays strike a crystalline sample it undergoes elastic scattering from the atoms in the crystalline material.

The interference between these scattered X-rays leads to a diffraction pattern which is unique to each material and can be considered as analogous to the fingerprint of a material. The constructive interference between these X-rays from the atoms in parallel lattice planes are seen as peaks in the diffraction pattern. The condition for constructive interference is given by Bragg's law,

$$n\lambda = 2d \sin\theta$$

where 'λ' is the wavelength of the incident X-ray, 'θ' is the scattering angle, 'n' is the order of reflection and 'd' is the inter-planar distance for a given set lattice planes. [45]

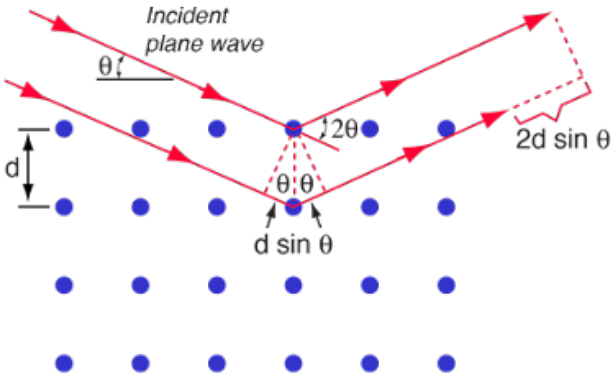

Figure 2.1: Figure illustrates the reflection of X-rays by lattice planes separated by distance 'd'. The scattered X-rays only interfere constructively if they satisfy the Bragg's condition given above.[46]

Bruker D8 Advance Powder X-ray Diffractometer facility at IISER Pune was used to check the phase of the samples after heat treatment. It has Bragg-Brentano geometry where the source and the detector can move in the entire 2θ range but the sample orientation is fixed. It produces Cu k_α X-rays with wavelength of 0.15406 nm. Before loading the sample into the Diffractometer the sample was ground properly to ensure random orientation of crystalline planes. The primary analysis of the XRD profile was done by matching the diffraction data obtained to the data from the International Centre for Diffraction Data (ICSD).

2.3 Structural Analysis

Structural analysis of the synthesized compounds were done using Rietveld refinement[47]. The method is based on least square fitting where refinement is carried out in an iterative manner where various parameters like background, lattice parameters, atomic positions, thermal parameters, instrumental parameters, profile parameters etc

are optimised. During refinement the program tries to minimize the function given by

$$\mathbf{G_y} = \sum_{\mathbf{i}} \mathbf{w_i}(\mathbf{y_i} - \mathbf{y_{ci}})$$

where,

$\mathbf{y_i}$ = Measured intensity at the i^{th} step

$\mathbf{y_{ci}}$ = Calculated intensity at the i^{th} step

$\mathbf{w_i} = \mathbf{1}/\mathbf{y_i}$

Calculated intensity $\mathbf{y_{ci}}$ depends on the square of the structure factor, $\mathbf{F_{hkl}}$ given by ,

$$\mathbf{F_{hkl}} = \sum_i N_i f_i e^{2\pi i(hx_i+ky_i+lz_i)} e^{-8\pi^2 u_s^2 \sin^2\theta/\lambda^2}$$

Here h,k,l are the Miller indices of a Bragg reflection,

x_i, y_i, z_i are the atomic positional parameters of the i_{ith} atom,

N_j is the site occupancy of the i_{ith} atom

f_j is the atomic scattering factor of the i_{ith} atom,

u_s^2 is the root mean square of the thermal displacement of i_{ith} atom in direction parallel to the diffraction vector.

The intensity of the i_{ith} step is calculated from the $\left|\mathbf{F_{hkl}}\right|^2$ values of given structural model and background intensity at the i_{ith} position.

$$\mathbf{y_{ci}} = S \sum_n L_n \left|F_{hkl}\right|^2 \phi\,(2\theta_i - 2\theta_n)\, P_k A + \mathbf{y_{bi}}$$

, where

S is the Scale factor

h,k,l are the Miller indices for a Bragg reflection,

L_k is the Lorentz polarization and multiplicity factor,

ϕ = is the Bragg reflection profile function,

P_k is the Preferred orientation function,

A is the absorption factor,

F_{hkl} is Structure factor corresponding to the Bragg reflection from hkl plane,

$\mathbf{y_{bi}}$ is the background intensity at i^{th} step

Since the function to be minimized is non-linear, the solution must be found by an iterative procedure. Also inputting a reasonable starting model is necessary in order to avoid any divergence or leading to a local minima. Now the Full-Width-at-Half-Maxima is given by,

$$H^2 = u\tan^2\theta + v\tan\theta + w$$

, where u,v,w are refinable parameters and H is the breadth of a Bragg reflection. The quality of the fit is determined by the R values. Among several R values present the most reliable one is the R_{wp}.

$$R_{wp} = \left[\frac{\sum \mathbf{i} w_i \left| y_i - y_{c,i} \right|^2}{\sum_i w_i y_i^2} \right]^{1/2}$$

Another criterion on the basis of which the fit can be judged on is the 'goodness of fit' parameter Z,

$$Z = \frac{R_{wp}}{R_e}$$

R_e is the Expected weighted profile factor, given by

$$R_e = \left[\frac{n - p}{\sum_i w_i y_i^2} \right]^{1/2}$$

Here n-p represents the number of degrees of freedom, where n is the number of points in the pattern minus the excluded points and p is the number of refined parameters.

A goodness of fit under 2 is generally regarded as being acceptable. Here the Pseudo Voigt function was used to fit the peak shape and Fullprof software was used for Rietveld refinement. [48]

2.4 Field Emission Scanning Electron Microscopy and Energy Dispersive X-Ray Spectroscopy

Field Emission Scanning Electron Microscopy(FESEM) provides high resolution images of the topography of a material. The working principle is as follows, electrons are ejected from a field emission source and these electrons are then accelerated via a high electric field gradient[49]. These electrons are called primary electrons and these primary electrons are then focused on to the sample with the help of lenses. This bombardment of the surface of the sample with primary electrons leads to ejection of electrons from the surface of the specimen and these are called secondary electrons. The velocity and angle of these secondary electrons are related to the morphology of the sample. A detector collects these secondary electrons converts it into an electronic signal which is further amplified and processed into a 3D image.[50]

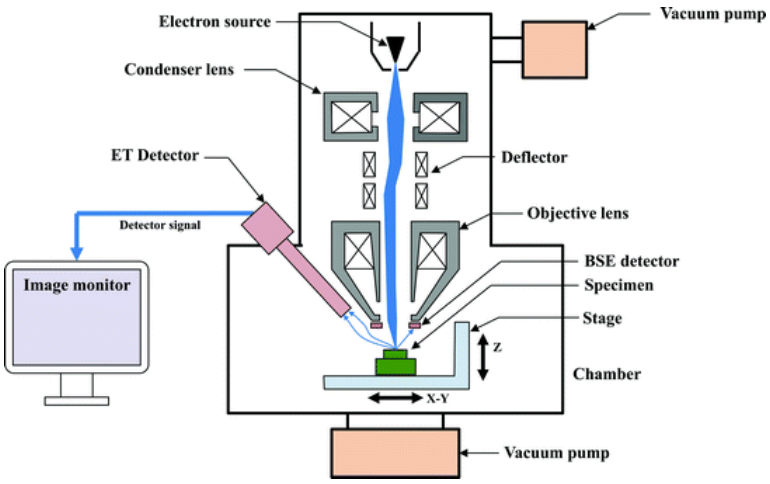

Figure 2.2: Figure shows a schematic of FESEM[51]

Energy Dispersive X-Ray Spectroscopy is a technique which helps in finding the elemental composition of a material. EDXS systems are attached to SEM instruments which help focus on the area of interest. In EDXS the specimen in bombarded with high energy electrons which excite the inner shell electrons in the specimen. Therefore a hole is created and an electron from a higher energy fills this hole created and in the process emitting X-Rays. The detector converts the individual X-rays into electric voltage and the composition is determined from this integrated intensity of each peak, given each element in the periodic table has a characteristic line energy.

2.5 Sputtering

Sputtering is one of the most popular methods to coat thin layer of a substance onto another material. The method involves placing a substrate which is to be coated in a vacuum chamber. The chamber is filled with an inert gas, mostly Argon and a negative charge is applied to the target material. A plasma plume is formed which interacts with the argon atoms in the vacuum chamber ionizing it. These positively charged Argon ions are attracted toward the negatively charged target material and will strike the target at high velocities leading to ejection of atoms from the target which then gets deposited on top of the substrate. The kinetic energy of these Argon ions need to be very high in order to ”sputter” atoms from the surface of the target[52]. The rate of this sputtering process can be increased by by placing magnets behind the target so as to trap over the negatively charged target such that they are not able to bombard the surface of the substrate. This method were magnets are used to control the rate of deposition is called Magnetron Sputtering, which was what we used to deposit our Pt layer.

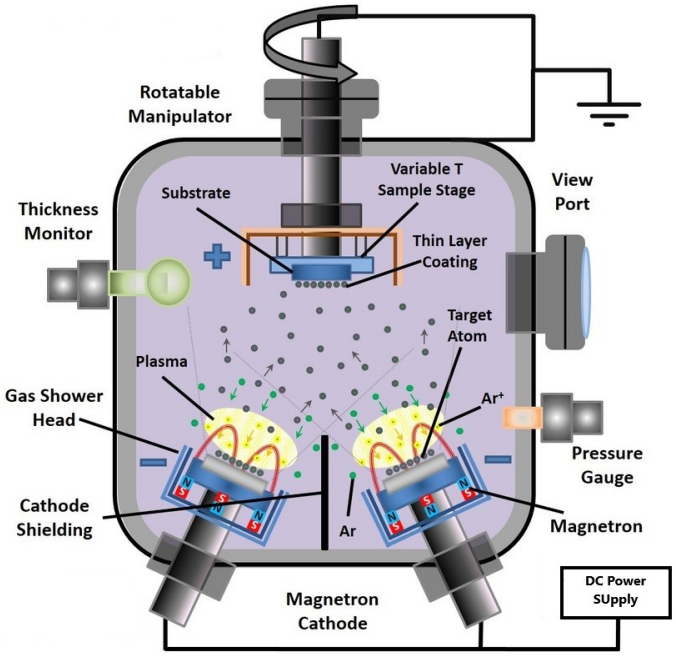

Figure 2.3: Figure shows a schematic of the working of a DC Magnetron sputtering system[53]

In order to measure Spin-Seebeck signal we made pellets out of the different samples and then cut and shaped these pellets into thin rectangular slabs. Then a thin bar of Pt with a thickness of around 20nm was coated on top of the slab. The Pt was deposited on to the slab using Sputtering using a mask on top the slab in order for the Pt to be deposited along the length of the slab in the shape of a small rectangular bar as shown in fig. 1.4.

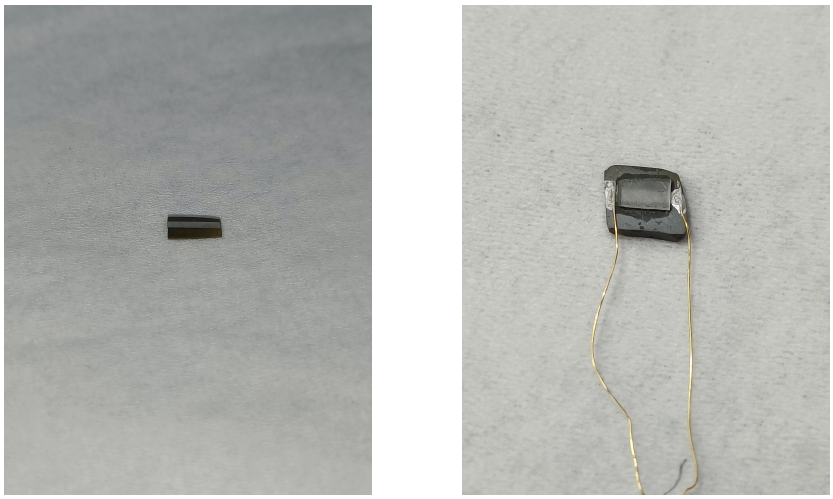

(a) (b)

Figure 2.4: (a) Shows Pt bar coated on top of GdIG slab. (b)Here two gold wires are attached to the ends of the Pt bar using Silver paste and a sapphire plate is cut such that it just covers the Pt bar in between the contacts. This sapphire plate is placed on top of the slab using Apiezon grease.

2.6 Atomic Force Microscopy (AFM)

Atomic Force Microscope[54] is a powerful imaging technique that is a type of Scanning probing microscopy and can be used to visualise the topography of materials on a nano-scale regime. The principle behind AFM is that a nanoscale tip is attached to a small cantilever. As the tip touches the surface of the specimen the cantilever bends and this can be detected using a laser diode and a photo-detector. The bending of the cantilever can be related to the interaction force.[55]

In order to measure the thickness of the Pt coating that was deposited, we first calibrated the Magnetron sputtering system with by placing SiO_2 as substrate. Then thickness of the deposited layer was measured using Atomic Force Microscopy (AFM), which was set in contact mode.

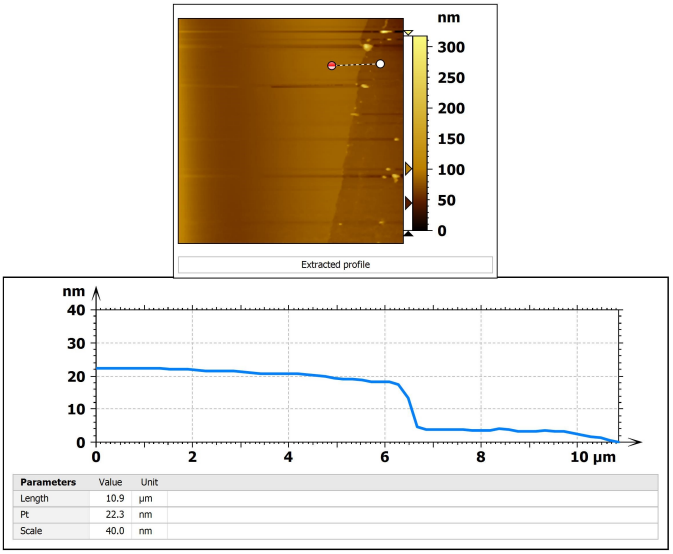

Figure 2.5: AFM image obtained for GdIG shows thickness of Pt layer deposited is roughly 20nm

2.7 Spin Seebeck Measurement Unit

The Longitudinal Spin Seebeck (LSSE)[25] Signal from the sample slabs prepared were measured on a home made apparatus. The set up consists of a closed cycle refrigerator(CCR from Advanced Research Systems model number: DE202), a temperature controller(model number: Lakeshore 336), a nanovoltmeter, a source meter, and an electromagnet with an upper field limit of 2 kOe. The temperature gradient across the sample and also the average temperature of the sample is controlled by two PID controlled heaters and the temperature is measured by two temperature sensors attached near the sample edge. The geometry of the holder is such that the applied thermal gradient is always orthogonal to the rotation plane of the magnetic field. The whole set-up is put inside a Faraday cage for reducing the noise, and signals as low as 10 nV can be reliably measured.

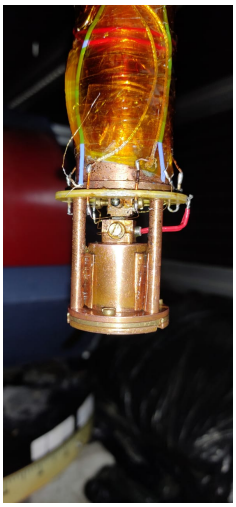

(a)

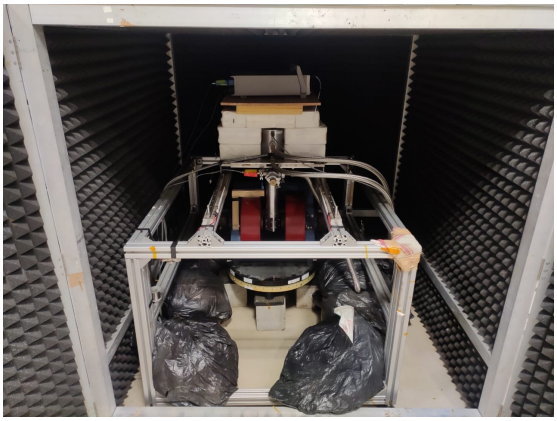

(b)

Figure 2.6: (a) Shows the sample holder onto which the prepared slab is loaded. (b)The SSE measurement set up is placed inside a Faraday cage in order to minimize noise.

Chapter 3

Results And Discussion

3.1 Structural Analysis

3.1.1 Gadolinium Iron Garnet(GdIG) - $Gd_3Fe_5O_{12}$

The synthesis was done according to the protocol mentioned in chapter 2. FESEM[56][45] images were taken post synthesis and are depicted in figure 3.1

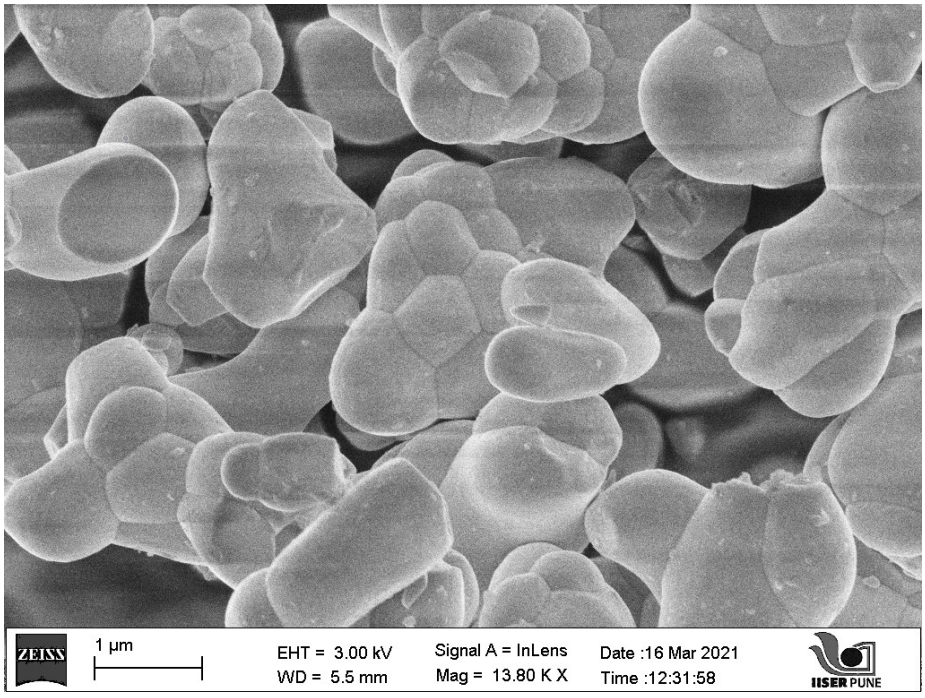

Figure 3.1: FESEM images showing micron sized crystallites of GdIG

The structural analysis of the XRD data obtained was done via the Rietveld method[47][57] using the Fullprof software[48]. The structural parameters obtained post refinement are given in Table 3.1.

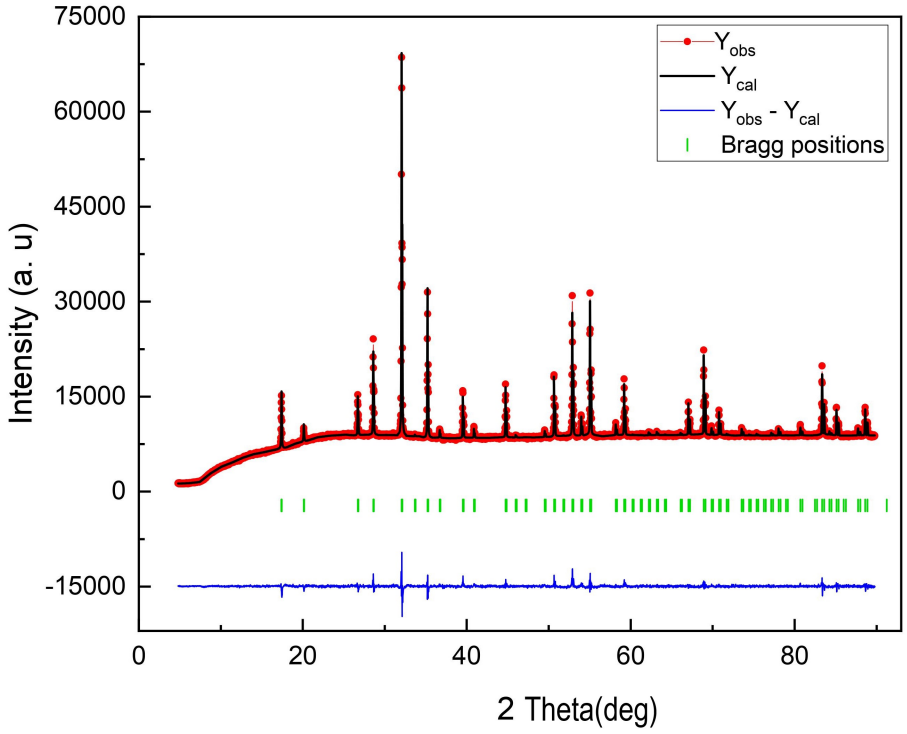

Figure 3.2: Rietveld plot for $Gd_3Fe_5O_{12}$

Chemical Formula	$Gd_3Fe_5O_{12}$
Molecular weight, g/mol	942.973
Temperature, K	296
Crystal Structure	Cubic
Space group symmetry and number	$Ia3d$, 230
Unit cell parameters	
a ,b, c (Å)	12.476
α, β, γ (deg)	90
Volume ($Å^3$)	1942.0122
Diffraction angle range (θ deg)	5-90
Step size (θ deg)	0.0196
$\mathbf{R_{wp}}$	15.1
$\mathbf{R_e}$	7.97
Chi_2	3.57
Goodness of fit ($\frac{R_{wp}}{R_e}$)	1.97

Table 3.1: Lattice and fitting parameters of $Gd_3Fe_5O_{12}$ obtained from Rietveld refinement

Atom	x/a	y/b	z/c	Fractional occupancy
Fe1	0	0	0	1.013
Fe2	0.375	0	0.25	1.012
Gd1	0.125	0	0.25	1
O1	0.15	-0.03529	0.05754	1

Table 3.2: Refined atomic positions and fractional occupancy

3.1.2 $Gd_3Fe_{4.96}Mn_{0.04}O_{12}$ (GdMnIG 4% Mn doped)

The synthesis of GdMnIG(4%) required heat treatments like oxygen atmosphere in order to avoid any oxygen deficiencies and also to prevent the raw material Mn_2O_3 from being reduced to Mn_3O_4 owing to the oxygen deficiency at high temperatures.[58]

$$6Mn_2O_3 = 4Mn_3O_4 + O_2 \uparrow$$

Also pure phase was only obtained after two heat treatments, the first one for 10hrs at 1200^oc and the second for 24hrs at 1200^oc. After the second heat treatment all the extra peaks which did not correspond to any of the parent GdIG peaks were removed(fig13.3). Furthermore a clear shift in the position of the peaks was observed, indicating a change in the lattice parameters. Therefore it can be inferred that Mn that was doped has indeed gone into the parent GdIG.

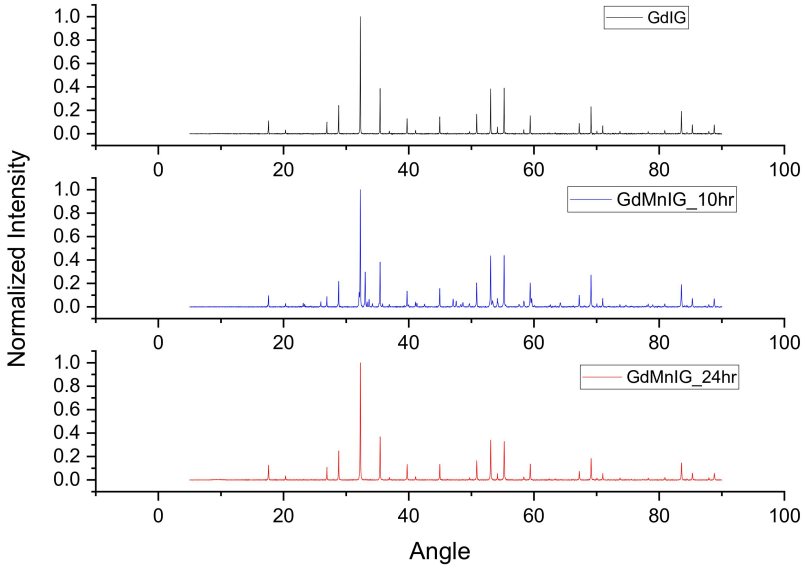

Figure 3.3: Shows the XRD data obtained for GdIG and GdMnIG(4%). Here we can see extra peaks after the 10hr heat treatment indicating that the pure phase has not formed but these were removed upon a further 24hr heat treatment

Chemical Formula	$Gd_3Fe_{4.96}Mn_{0.04}O_{12}$‘1
Molecular weight, g/mol	942.938
Temperature, K	296
Crystal Structure	Cubic
Space group symmetry and number	$Ia3d$, 230
Unit cell parameters	
a ,b, c (Å)	12.47541
α, β, γ (deg)	90
Volume (Å^3)	1941.623
Diffraction angle range (θ deg)	5-90
Step size (θ deg)	0.0196
$\mathbf{R_{wp}}$	10.4
$\mathbf{R_e}$	5.68
Chi_2	3.39
Goodness of fit ($\frac{R_{wp}}{R_e}$)	1.83

Table 3.3: Lattice and fitting parameters of $Gd_3Fe_{4.96}Mn_{0.04}O_{12}$ obtained from Rietveld refinement

Atom	x/a	y/b	z/c	Fractional occupancy
Fe1	0	0	0	1.0123
Fe2	0.375	0	0.25	1.02
Mn1	0	0	0	0.4
Mn2	0.375	0	0.25	0.6
Gd1	0.125	0	0.25	1
O1	0.15	-0.03529	0.05754	1

Table 3.4: Refined atomic positions and fractional occupancy

The XRD data obtained post the second heat treatment was refined via the Rietveld

method. Considerations pertaining to the occupancy were made during the refining phase. Here the doping of Mn is on the Iron site, but since there are two different types of Iron sites in our unit cell, namely a tetrahedral site and an octahedral site, it needs to be ascertained as to which the doped Mn atom would occupy. For this refinement was carried out via two different routes. The first one had all of the Mn sit in the tetrahedral site and the in the second route we started out with 50% of the doped Mn in the tetrahedral site and the other 50% in the octahedral and then the occupancies were refined. Here the chi^2 for the refinement having all of the Mn in the tetrahedral site was 3.91 and in the case of partial occupancy of Mn in both the tetrahedral and octahedral site, the χ^2 was 3.38. This indicates that the model with partial Mn doping on the octahedral and tetrahedral site was a better fit. Also upon refining the occupancies of Mn at the octahedral and tetrahedral site, a slightly higher value was obtained for the tetrahedral site indicating that at 4% doping the Mn has greater occupancy at the tetrahedral site. The detailed structural parameters are given below in table 3.3 and 3.4

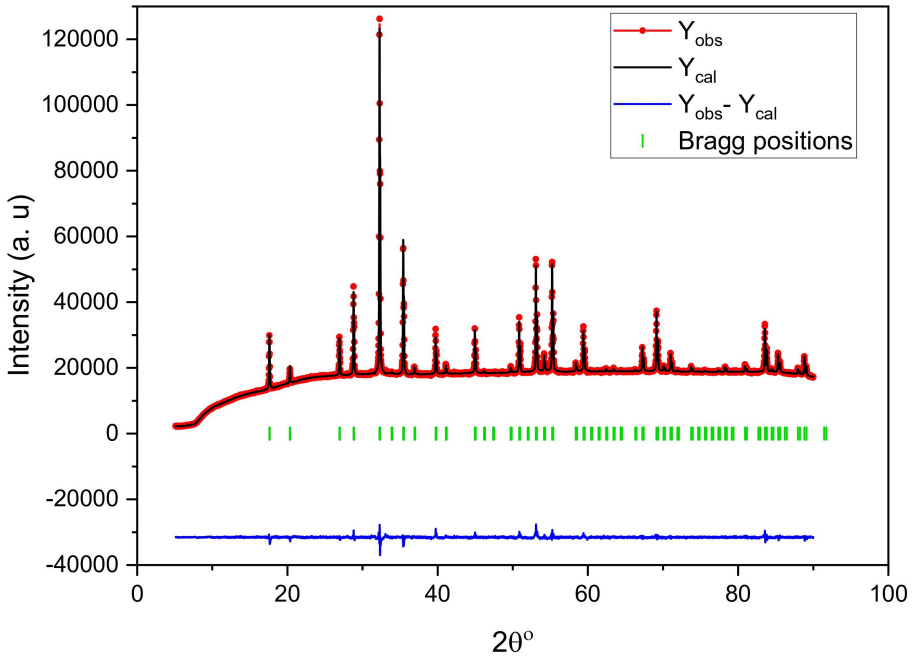

Figure 3.4: Rietveld refinement fit for $Gd_3Fe_{4.96}Mn_{0.04}O_{12}$

3.1.3 $Gd_3Fe_{4.92}Mn_{0.08}O_{12}$ (GdMnIG 8% Mn doped)

During the synthesis of GdMnIG(8%) the reaction was done using a platinum crucible in order to eliminate the alumina contamination that was plaguing the trial runs of the sample.With the use of Pt crucible even though the percentage of alumina in the sample seems to have reduced there was still a very small alumina peak found, with the intensity of the peak corresponding to around 1 percent of largest parent peak, which

leads us to believe that there may have been some other external source of alumina contamination . Furthermore unlike in the case of GdMnIG(4%) only one 10hr oxygen treatment at 1200^{o}c was required to get a relatively clean phase, not considering the small alumina peak.

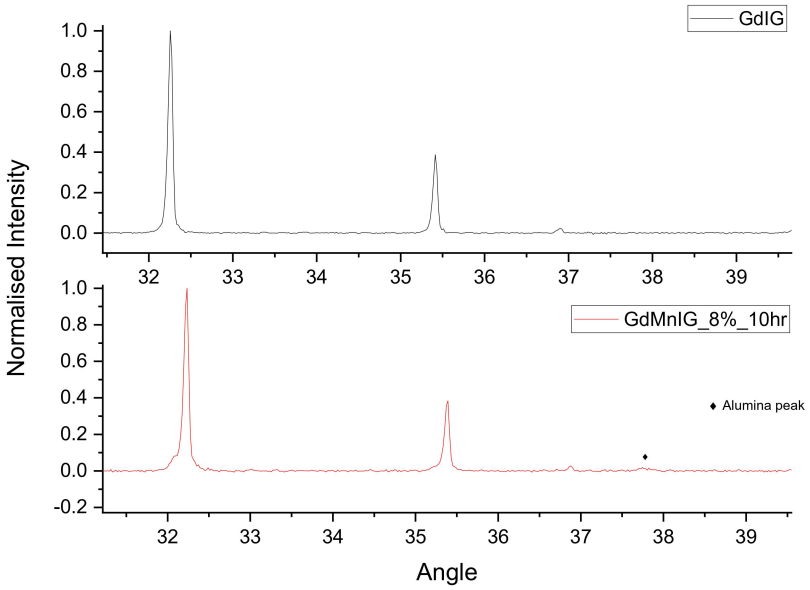

Figure 3.5: On comparing the XRD data of GdMnIG(8%) with that of GdIG we can see that there is a small extra peak which was suspected to be that of alumina.

Chemical Formula	$Gd_3Fe_{4.92}Mn_{0.08}O_{12}$
Molecular weight, g/mol	941.300
Temperature, K	296
Crystal Structure	Cubic
Space group symmetry and number	$Ia3d$, 230
Unit cell parameters	
a ,b, c (Å)	12.47544
α, β, γ (deg)	90
Volume (Å^3)	1941.6079
Diffraction angle range (θ deg)	5-90
Step size (θ deg)	0.0196
$\mathbf{R_{wp}}$	22.4
$\mathbf{R_e}$	8.5
Chi^2	6.94
Goodness of fit ($\frac{R_{wp}}{R_e}$)	2.635

Table 3.5: Lattice and fitting parameters of $Gd_3Fe_{4.92}Mn_{0.08}O_{12}$ obtained from Rietveld refinement. Comparing the unit cell parameters of $Gd_3Fe_5O_12$ with that of $Gd_3Fe_{4.96}Mn_{0.04}O_{12}$ and $Gd_3Fe_{4.92}Mn_{0.08}O_{12}$ we can see a decrease in the unit cell parameter magnitudes with increasing concentrations of Mn doping.

Atom	x/a	y/b	z/c	Fractional occupancy
Fe1	0	0	0	0.3408
Fe2	0.375	0	0.25	0.4831
Mn1	0	0	0	0.036
Mn2	0.375	0	0.25	0.36
Gd1	0.125	0	0.25	0.9978
O1	0.15	-0.03529	0.05754	1

Table 3.6: Refined atomic positions and fractional occupancy. Here the occupancies of Mn1, Mn2, Fe1, and Fe2 are not exactly consistent with the theoretical predictions. This may be attributed to the presence of the alumina in the sample which maybe influencing the refinement

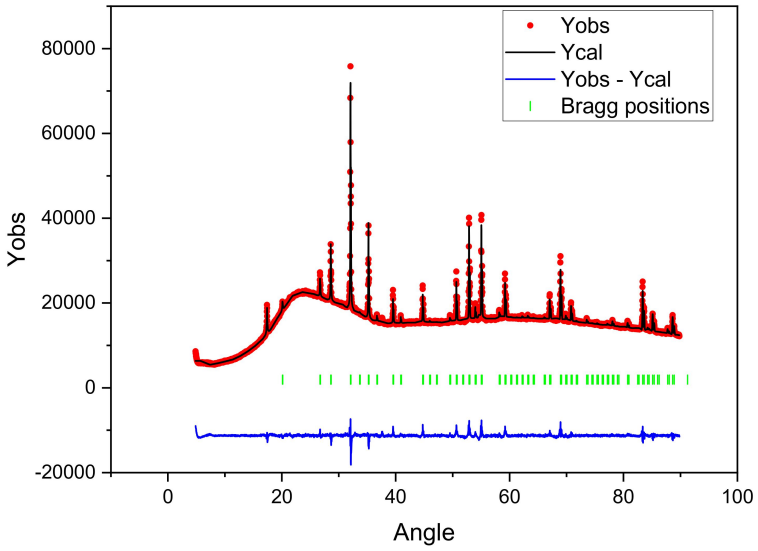

Figure 3.6: Rietveld fitting profile of $Gd_3Fe_{4.92}Mn_{0.08}O_{12}$.

3.1.4 $Gd_3Fe_{4.9}Mn_{0.1}O_{12}$ (GdMnIG 10% Mn doped)

Synthesis of GdMnIG(10%) was also attempted. But here even though the GdIG phase seems to have formed a sizable peak corresponding to alumina was also observed along with a a minor peak corresponding to a compound of both ”Al” and ”Mn”. The presence of these peaks is suspected to be due to the reaction of our sample with the alumina crucible used for the reaction. Also due to the presence of these somewhat major impurity peaks in the sample, Rietveld refinement could not be done on the sample.

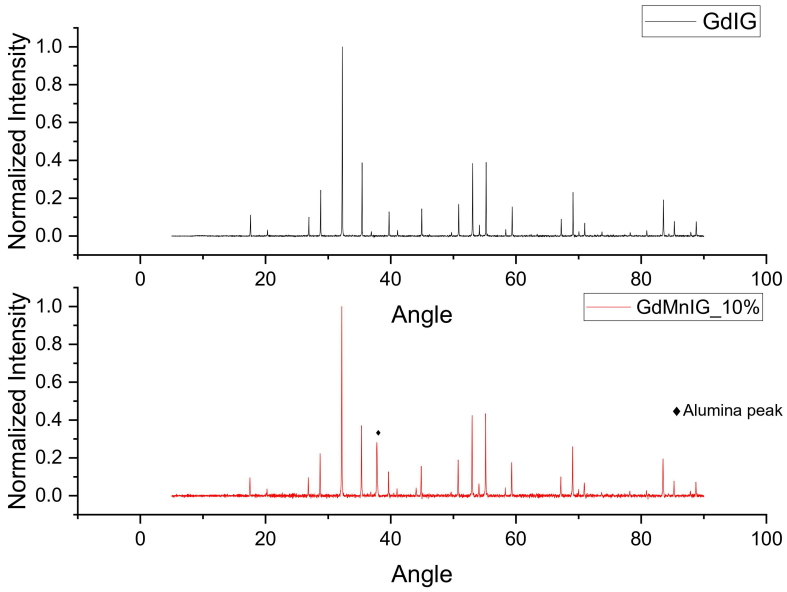

Figure 3.7: XRD data of $Gd_3Fe_{4.9}Mn_{0.1}O_{12}$ shows a very major impurity peak of alumina, with a relative intensity of almost 30 percent with respect to the largest parent peak.

3.1.5 Ytterbium Iron Garnet - $Yb_3Fe_5O_{12}$

The synthesis of YbIG invovlved three heat treatments; the first at 1200^oc for 10hrs, the second at 1200^oc for another 24hrs and then a final 10hr heat treatment at 1200^oc in oxygen atmosphere. The XRD of the sample was taken post each sintering stage.

After the first heat treatment there were still a few extra peaks that did not correspond to any of the parent compound. Hence the sample was heated fora further 24hrs. Post this second heat treatment, the XRD data was observed and even though no rogue peaks were found, all the peaks were accompanied by a left side shoulder peak. There the sample was subjected to heat treatment of 10hrs in oxygen atmosphere. And post this treatment YbIG was formed in pure phase.

The Rietveld refinement was done(fig) on the XRD data obtained and structural parameters of YbIG were found.

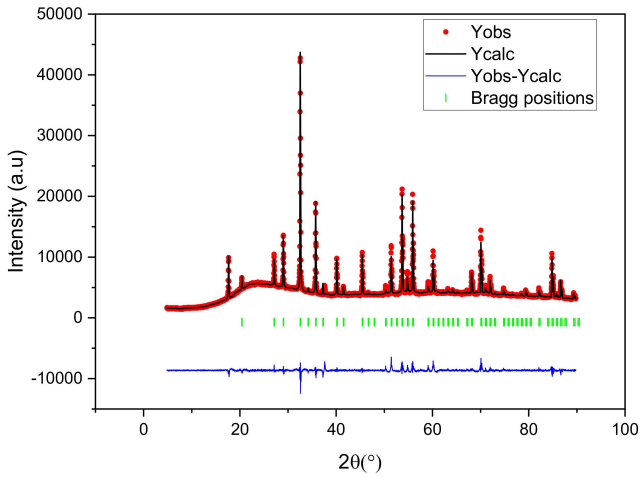

Figure 3.8: Rietveld refinement fit for $Yb_3Fe_5O_{12}$

Chemical Formula	$Yb_3Fe_5O_{12}$
Molecular weight, g/mol	990.333
Temperature, K	296
Crystal Structure	Cubic
Space group symmetry and number	*Ia3d*, 230
Unit cell parameters	
a ,b, c (Å)	12.296
α, β, γ (deg)	90
Volume (Å^3)	1860.8523
Diffraction angle range (θ deg)	5-90
Step size (θ deg)	0.0196
R_{wp}	18.1
R_e	7.25
Chi^2	6.24
Goodness of fit ($\frac{R_{wp}}{R_e}$)	2.49

Table 3.7: Lattice and fitting parameters of $Yb_3Fe_5O_{12}$ obtained from Rietveld refinement.

Atom	x/a	y/b	z/c	Fractional occupancy
Fe1	0	0	0	1.0042
Fe2	0.375	0	0.25	1.0376
Yb1	0.125	0	0.25	1.0084
O1	0.15	-0.03529	0.05754	1.56

Table 3.8: Refined atomic positions and fractional occupancy of YbIG

3.1.6 Yttrium Iron Garnet(YIG) - $Y_3Fe_5O_{12}$

The synthesis protocol for YIG was similar to the one used for YbIG and required three heat treatments, the third one being in oxygen atmosphere which was done in order to get rid of any oxygen deficiency in the sample. The structural details obtained via Rietveld refinement are given below.

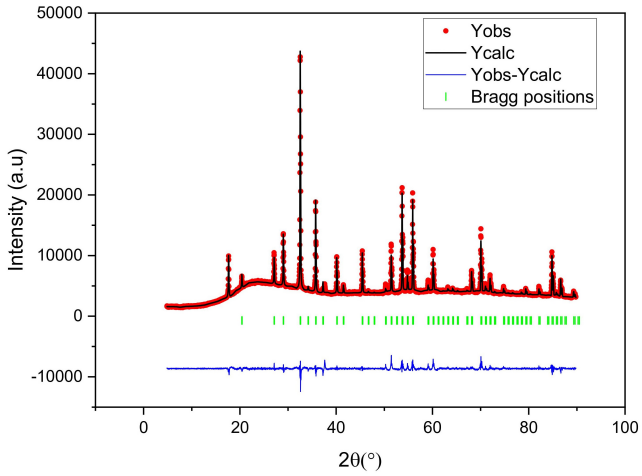

Figure 3.9: Rietveld refinement fit for $Y_3Fe_5O_{12}$

Chemical Formula	$Y_3Fe_5O_{12}$
Molecular weight, g/mol	737.9304
Temperature, K	296
Crystal Structure	Cubic
Space group symmetry and number	*Ia*3*d*, 230
Unit cell parameters	
a ,b, c (Å)	12.376
α, β, γ (deg)	90
Volume (Å^3)	1895.478
Diffraction angle range (θ deg)	5-90
Step size (θ deg)	0.0196
R_{wp}	16.3
R_e	5.86
Chi^2	7.702
Goodness of fit ($\frac{R_{wp}}{R_e}$)	2.78

Table 3.9: Lattice and fitting parameters of $Y_3Fe_5O_{12}$ obtained from Rietveld refinement.

Atom	x/a	y/b	z/c	Fractional occupancy
Fe1	0	0	0	1.0186
Fe2	0.375	0	0.25	1.0077
Yb1	0.125	0	0.25	1.0084
O1	0.15	-0.03529	0.05754	0.9885

Table 3.10: Refined atomic positions and fractional occupancy of YIG

3.2 Spin Seebeck Measurements

The spin Seebeck signal measurements on GdIG, GdMnIG(4%) and YbIG were carried out using a home made set. The results are given below.

3.2.1 GdIG

A GdIG/Pt device was fabricated on top of which a 20nm thick layer of Pt was deposited via sputtering. The length and thickness of the slab was measured to be 2.45mm and 0.84mm respectively and resistance at room temperature of the deposited Pt bar was found to be 1.48 kΩ

The normalised spin Seebeck voltage is given by :

$$V_{LSSE} = \frac{V'_{\text{Total}} * L_z}{\Delta T * R'_{\text{Total}} * L_y}$$

Where ΔT is the applied temperature gradient, L_y is the length of the Pt bar deposited on the slab, R'_{Total} is the resistance of the slab at a given temperature, and V'_{Total} is total measured signal.

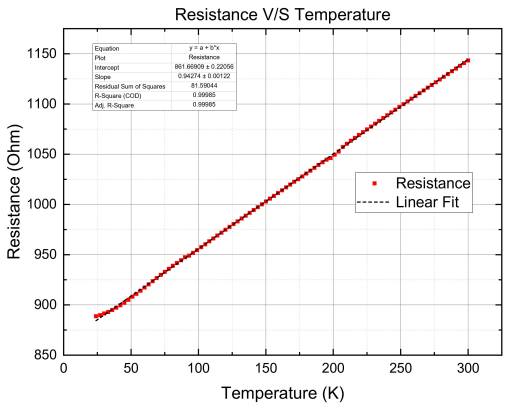

Figure 3.10: Figure shows the zero field temperature dependent resistance measurements done on GdIG/Pt slab. The resistance shows a linear trend with y-intercept = 861.669 ± 0.221 and slope 0.9427 ± 0.0012

The SSE signal was measured as a function of temperature and we observed that presence of two transition points where the strength of the signal went to zero (fig3.11).This is consistent with reported temperature dependent SSE signal study on GdIG/Pt thin film[35].

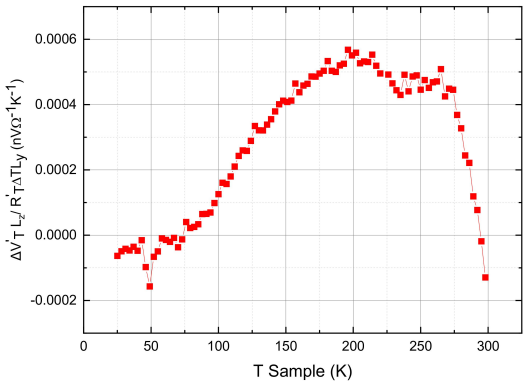

Figure 3.11: Figure shows temperature dependence of the SSE signal with temperature. Here we can clearly see the two transition points where the sign of the signal has flipped. Other than the two transition points we can see that signal value peaks at around 200K, this peak in intensity can be attributed to the magnon population and magnon lifetimes.

Here the first transition point at around 290K can be explained on the basis of the flipping of the sublattice magnetisation at the compensation temperature, T_{comp}. The origin of the second transition point close to 75K is not as clear but is suspected to be due to the different temperature dependences of the spin wave power spectral densities and/or different exchange coupling strengths of these modes at the GdIG/Pt interface.[35]

The SSE signal was measured at both 200K and 300K with a ΔT of 20K in both cases and the plots are given below.

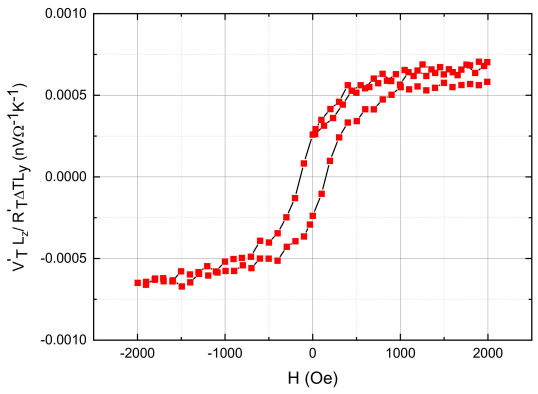

Figure 3.12: Figure shows the hysteresis of the spin Seebeck signal of $Gd_3Fe_5O_{12}$ measured at 200K with a ΔT of 20K. The signal saturates at around 1500 Oe. The fact that the loop doesn't exactly close can be attributed to a shift in the background.

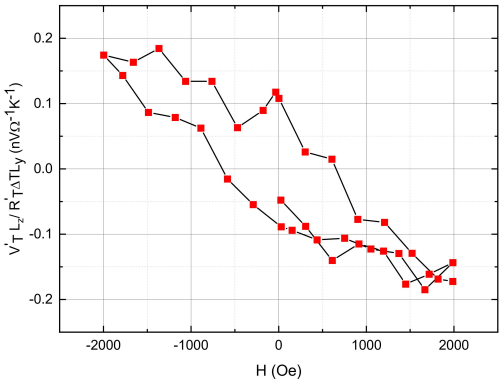

Figure 3.13: Figure shows the hysteresis of the spin Seebeck signal of $Gd_3Fe_5O_{12}$ measured at 300K with ΔT of 20K.Here the overall signal strength is considerably less than that at 200K and polarity of the signal is also flipped, this can be explained on the basis of the reversal of the sublattice magnetisation at T_{comp}.

3.2.2 GdMnIG 4% Mn Doped

As in the case of GdIG, a GdMnIG(4%) slab was fabricated via sputtering, where a 20nm Pt bar was deposited along the length of the slab. The resistance at room temperature of the deposited Pt bar was measured to be roughly 400 Ω and the length and thickness of the slab used were 5.8mm and 0.58mm respectively.

Similar measurements like in the case of GdIG were carried out with GdMnIG as well. Here in the case of the temperature dependent SSE signal, we observe a similar trend to that seen in GdIG slab measurements. There appears to be two transition points, the first at around 75K is due to increased contribution of the β-magnon mode at higher temperatures. The second transition point which is due to the magnetic compensation can't exactly be reached within the limits of our instruments, but the trend clearly indicates the a T_{comp} to be higher than 300K. fig 3.14

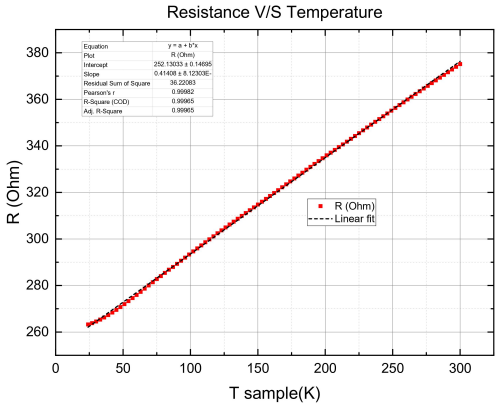

Figure 3.14: Figure shows the zero field temperature dependent resistance measurements done on GdIG/Pt slab. The resistance shows a linear trend with y-intercept = 252.1303 ± 0.1489 and slope 0.4141 ± 0.0008

This increase in the T_{comp} of $Gd_3Fe_{4.96}Mn_{0.04}O_{12}$ compared to that of $Gd_3Fe_5O_{12}$ is due to the partial substitution of the octahedral Fe atom by the doped Mn, because the total magnetisation of the lattice is determined by the individual sublattice magnetisation which are highly temperature dependent. In $Gd_3Fe_5O_{12}$, the Gd magnetic sublattice and tetrahedral Fe sublattice are weakly exchange coupled and hence exhibit magnetisation along the same direction. Whereas the tetrahedral and octahedral Fe sublattices are antiferromagnetically coupled via super exchange interaction[35]. So when Mn^{+3} which has a magnetic moment less than Fe^{+3}, replaces Fe^{+3} in the octahedral site this leads to a decrease in the net magnetisation of the octahedral Fe sublattice. Furthermore the net magnetisation of the Gd and tetrahedral Fe sublattices increase with decrease in temperature and that of the octahedral Fe decreases with decrease in temperature, this combined with the initial decrease in the magnitude of the net magnetisation of the octahedral Fe sublattice leads to an increase in the compensation temperature, which is exactly what we have been able to observe here.

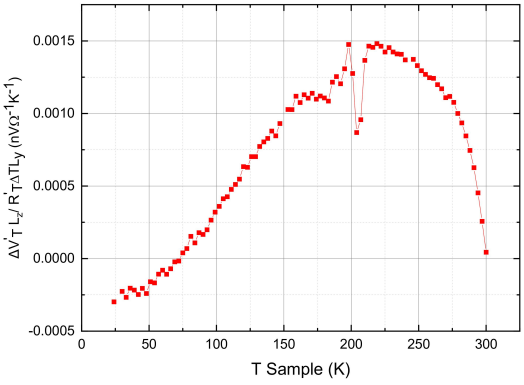

Figure 3.15: We can clearly see the two transitions points and also to be noted is that the signal strength peaks at around 210K which is around a +10K shift from what was observed in GdIG

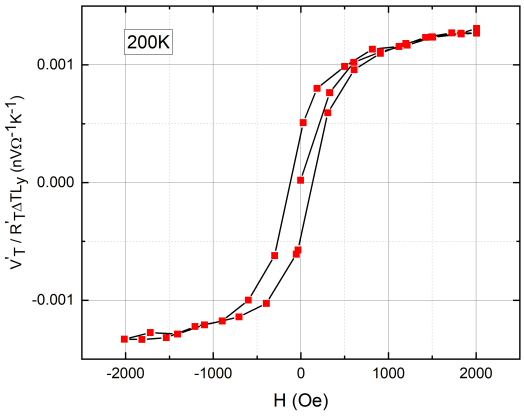

Figure 3.16: Figure shows the hysteresis of the spin Seebeck signal at 200K with a ΔT = 20K. The polarity of the signal is same as the one obtained for GdIG in the temperature regime where T < T_{comp}

A hysteresis loop for the SSE signal could not be traced at 300K due to the signal strength being very low because we are approaching T_{comp}, but also because the background kept shifting.

3.2.3 GdMnIG 8% Mn Doped

GdMnIG(8%) slab was fabricated via sputtering, where a 20nm Pt bar was deposited along the length of the slab. The resistance at room temperature of the deposited Pt bar was measured to be roughly 160 Ω and the length and thickness of the slab used were 4.18mm and 0.65mm respectively.

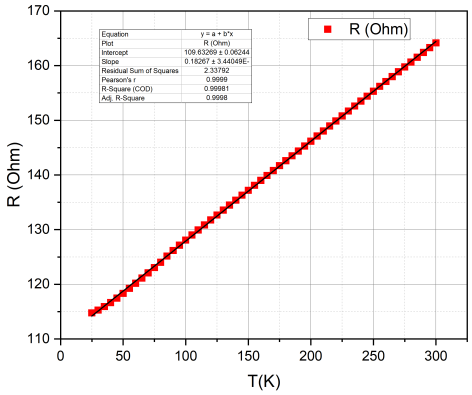

(a)

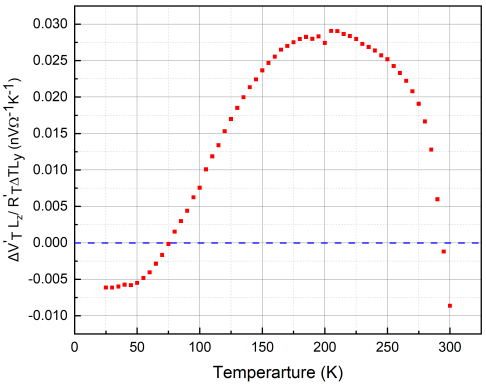

(b)

Figure 3.17: (a)Shows the zero field temperature dependent resistance measurements done on GdIG/Pt slab. The resistance shows a linear trend with y-intercept = 109.6327 ± 0.0624 and slope 0.1827 ± 0.0003. (b)There are two transition points like in the case of both GdIG and GdMnIG 4% doped samples. There is no real change in the second transition point as compared to the previous samples but there is a 5K decrease in the transition point from GdMnIG 4%

The 8% Mn doped sample showed a decrease in compensation temperature as compared to the 4% Mn doped sample. This is because the $Mn^{+}3$ ion prefers to occupy the tetrahedral site, due to certain tetrahedral stabilisation but at lower concentration of Mn doping there is also partial substitution into the octahedral site which is the case with the 4% sample. But as concentration of Mn increases this tendency of the Mn+3 ion to go into the octahedral site decreases and most of it diffuses into the tetrahedral site leading to a decrease in the compensation temperature, as is observed in our experiment.

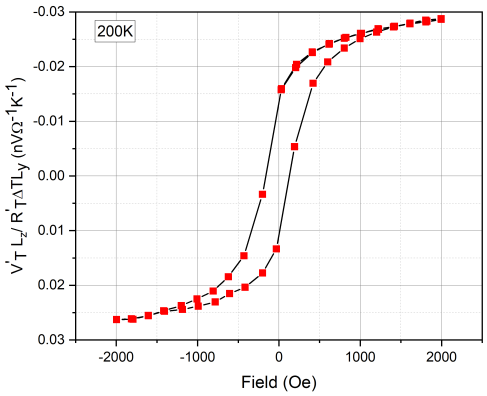

(a)

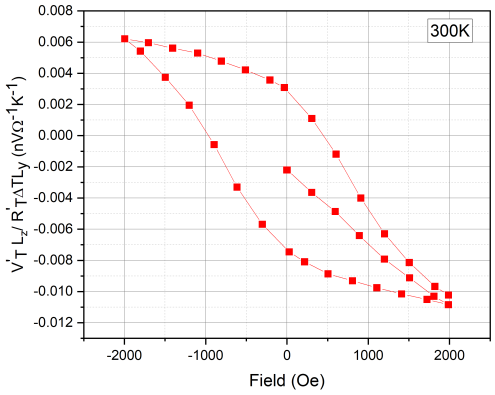

(b)

Figure 3.18: (a) and (b) Shows hysteresis of SSE signal at 200K and 300K respectively. The polarity of the signal is flipped due to spin reorientation at the compensation point.

Additionally it was observed that the strength of the SSE signal increased dramatically with Mn doping (Fig 3.19). The signal initially increased by 3 to 4 times with 4%

Mn doping compared to GdIG but increased by almost 80% compared to GdIG with 8% Mn doping. The reason for this is not precisely known.

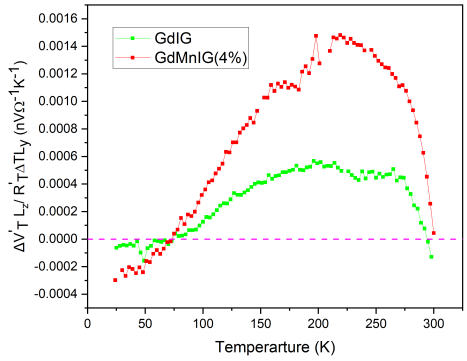

(a)

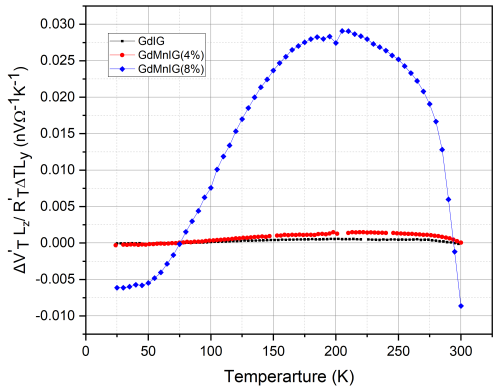

(b)

Figure 3.19: (a) Compares SSE signal strength of GdIG and 4% Mn doped GdMnIG and (b) Compares the SSE signal strength of GdIG, 4% Mn doped and 8% Mn doped GdMnIG. From (a) and (b) it can be clearly seen that with 8% Mn doping the signal strength is almost an order of magnitude greater than the other two.

3.2.4 $Yb_3Fe_5O_{12}$ - YbIG

YbIG slab was fabricated via sputtering, where a 20nm Pt bar was deposited along the length of the slab. The resistance between the contacts at room temperature was measured to be roughly 1 KΩ and the length and thickness of the slab used were 5.8mm and0.4mm respectively.

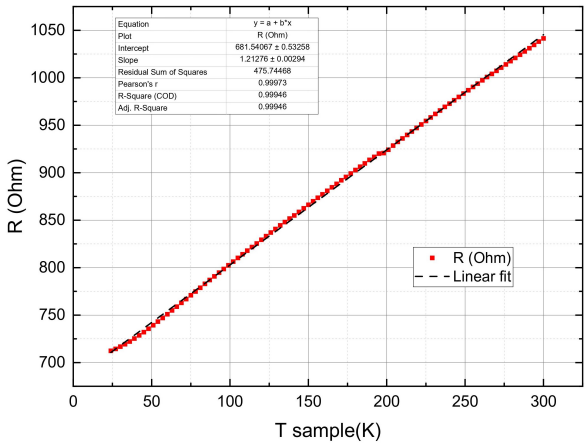

Figure 3.20: Figure shows the zero field temperature dependent resistance measurements done on YbIG/Pt device. The resistance shows a linear trend with y-intercept = 681.5407 ± 0.5326 and slope 1.2128 ± 0.0029

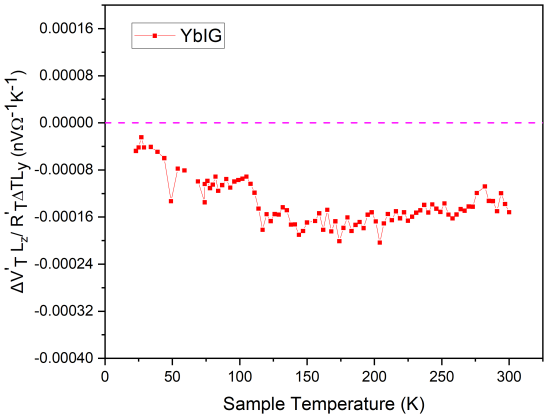

Figure 3.21: Figure shows the spin Seebeck voltage as a function of temperature

Fig 3.21 shows the spin Seebeck signal ΔV as a function of temperature. Here the signal has a nearly constant magnitude until around 100K, the reason for which is not entirely known. After 100K the signal starts to approach '0' with decrease in temperature. This can be attributed to the fact that the T_{comp} of YbIG is reported to be around 10K[59].

Chapter 4

Conclusions And Future Work

In summary the solid state synthesis of $Gd_3Fe_5O_12$(GdIG), $Y_3Fe_5O_{12}$(YIG), $Yb_3Fe_5O_{12}$(YbIG) and $Gd_3Fe_{5-x}Mn_xO_{12}$(x =0.04, 0.08) were completed. The synthesised garnets crystallise in a cubic structure with space group $Ia3d$.

The Spin Seebeck measurements were conducted on GdIG, GdMnIG(4%), GdMnIG(8%) and YbIG slabs on top of which a Pt bar coated via sputtering. From the spin Seebeck measurements it can be inferred that the T_{comp} of GdIG increased with 4% Mn doping. We were also able to reproduce the reported spin Seebeck signal trend for GdIG and could confirm the presence of a second transition point at a lower temperature, which is due to an increased contribution of the β-magnon mode at higher temperatures. There was also up to an order of magnitude increase in signal strength with Mn doping, the reasons for which are not clear.

The future phases of the project would entail the fabrication of GdIG and Mn doped GdIG thin films and the measurements of the spin Seebeck signal using these samples. Furthermore fabrication of hetero structure thin films made of GdIG and Mn doped GdIG can also be attempted, which could pave the way for the fabrication of a thermal spin diode.

References

1. Hirohata, A. **andothers**. Review on spintronics: Principles and device applications. *Journal of Magnetism and Magnetic Materials* **509,** 166711. ISSN: 0304-8853 (2020).
2. Diény, B. Giant magnetoresistance in spin-valve multilayers. *Journal of Magnetism and Magnetic Materials* **136,** 335–359 (1994).
3. Fert, A. & Van Dau, F. N. Spintronics, from giant magnetoresistance to magnetic skyrmions and topological insulators. *Comptes Rendus Physique* **20,** 817–831 (2019).
4. Baibich, M. N. **andothers**. Giant magnetoresistance of (001) Fe/(001) Cr magnetic superlattices. *Physical review letters* **61,** 2472 (1988).
5. *Spintronics materials* https://www.sigmaaldrich.com/IN/en/technical-documents/technical-article/materials-science-and-engineering/microelectronics-and-nanoelectronics/recent-progress-in-spintronic-materials.
6. *Spin caloritronics* http://users.physik.fu-berlin.de/ nunner/Research.html.
7. Saitoh, E., Ueda, M., Miyajima, H. & Tatara, G. Conversion of spin current into charge current at room temperature: Inverse spin-Hall effect. *Applied physics letters* **88,** 182509 (2006).
8. Adachi, H., Uchida, K.-i., Saitoh, E. & Maekawa, S. Theory of the spin Seebeck effect. *Reports on Progress in Physics* **76,** 036501 (2013).
9. Yang, T., Kimura, T. & Otani, Y. Giant spin-accumulation signal and pure spin-current-induced reversible magnetization switching. *Nature Physics* **4,** 851–854 (2008).
10. Barla, P., Joshi, V. K. & Bhat, S. Spintronic devices: a promising alternative to CMOS devices. *Journal of Computational Electronics* **20,** 805–837 (2021).
11. Maekawa, S., Valenzuela, S. O., Saitoh, E. & Kimura, T. *Spin current* (Oxford University Press, 2017).
12. Zhao, Y., Parshall, D., Ratcliff, W. & Lynn, J. Magnetic Phase Transition and Spin Wave Excitations in the Colossal Magnetoresistive Manganites: An Experiment Using the BT7 Triple-Axis Spectrometer.
13. Kimura, T., Hamrle, J. & Otani, Y. Estimation of spin-diffusion length from the magnitude of spin-current absorption: Multiterminal ferromagnetic/nonferromagnetic hybrid structures. *Physical Review B* **72,** 014461 (2005).

14. Hirsch, J. Spin hall effect. *Physical review letters* **83,** 1834 (1999).

15. Maekawa, S., Adachi, H., Uchida, K.-i., Ieda, J. & Saitoh, E. Spin current: Experimental and theoretical aspects. *Journal of the Physical Society of Japan* **82,** 102002 (2013).

16. Dyakonov, M. I. Spin Hall Effect. *International Journal of Modern Physics B* **23,** 2556–2565 (2009).

17. Sinova, J., Valenzuela, S. O., Wunderlich, J., Back, C. & Jungwirth, T. Spin hall effects. *Reviews of modern physics* **87,** 1213 (2015).

18. Feng, Y. P. **andothers**. Prospects of spintronics based on 2D materials: Spintronics Based on 2D Materials. *Wiley Interdisciplinary Reviews: Computational Molecular Science* **7,** e1313 (**april** 2017).

19. Ando, K. & Saitoh, E. Observation of the inverse spin Hall effect in silicon. *Nature communications* **3,** 1–6 (2012).

20. Uchida, K.-i. **andothers**. Observation of longitudinal spin-Seebeck effect in magnetic insulators. *Applied Physics Letters* **97,** 172505 (2010).

21. Arboleda, J. **andothers**. Evidence of the spin Seebeck effect in Ni-Zn ferrites polycrystalline slabs. *Solid State Communications* **270,** 140–146 (2018).

22. Uchida, K. **andothers**. Thermal spin pumping and magnon-phonon-mediated spin-Seebeck effect. *Journal of Applied Physics* **111,** 103903 (2012).

23. Huang, S.-M. Effect of thermal annealing on the spin Seebeck effect in Pt/Ni81Fe19 at room temperature. *Thin Solid Films* **631,** 200–204. ISSN: 0040-6090 (2017).

24. Miyasato, T. **andothers**. Crossover behavior of the anomalous Hall effect and anomalous Nernst effect in itinerant ferromagnets. *Physical review letters* **99,** 086602 (2007).

25. Uchida, K. **andothers**. Observation of the spin Seebeck effect. *Nature* **455,** 778–781 (2008).

26. Uchida, K.-i., Nonaka, T., Ota, T. & Saitoh, E. Longitudinal spin-Seebeck effect in sintered polycrystalline (Mn, Zn) Fe 2 O 4. *Applied Physics Letters* **97,** 262504 (2010).

27. Uchida, K. **andothers**. Electric detection of the spin-Seebeck effect in magnetic insulator in the presence of interface barrier. **303,** 012096 (**july** 2011).

28. Uchida, K. **andothers**. Longitudinal spin Seebeck effect: from fundamentals to applications. *Journal of Physics: Condensed Matter* **26,** 343202 (2014).

29. Ramos, R. **andothers**. Thermoelectric performance of spin Seebeck effect in Fe3O4/Pt-based thin film heterostructures. *APL Materials* **4,** 104802 (2016).

30. Yamamoto, A. **andothers**. Evaluation of correlation between orientation of Y 3 Fe 5 O 12 (YIG) thin film and spin Seebeck effect. *IEEE Transactions on Magnetics* **53,** 1–4 (2017).

31. Rezende, S. **andothers**. Magnon spin-current theory for the longitudinal spin-Seebeck effect. *Physical Review B* **89,** 014416 (2014).

32. Ando, K. **andothers**. Inverse spin-Hall effect induced by spin pumping in metallic system. *Journal of applied physics* **109,** 103913 (2011).

33. Urban, R., Woltersdorf, G. & Heinrich, B. Gilbert damping in single and multilayer ultrathin films: Role of interfaces in nonlocal spin dynamics. *Physical review letters* **87,** 217204 (2001).

34. Blundell, S. *Magnetism in condensed matter* 2003.

35. Geprägs, S. **andothers**. Origin of the spin Seebeck effect in compensated ferrimagnets. *Nature communications* **7,** 1–6 (2016).

36. Finley, J. & Liu, L. Spintronics with compensated ferrimagnets. *Applied Physics Letters* **116,** 110501 (2020).

37. Emori, S. & Li, P. Ferrimagnetic insulators for spintronics: Beyond garnets. *Journal of Applied Physics* **129,** 020901 (2021).

38. Yang, Y., Liu, T., Bi, L. & Deng, L. Recent advances in development of magnetic garnet thin films for applications in spintronics and photonics. *Journal of Alloys and Compounds* **860,** 158235 (2021).

39. Willoughby, A., Capper, P. & Kasap, S. *Spintronics for next generation innovative devices* (John Wiley & Sons, 2015).

40. Yang, Y., Liu, T., Bi, L. & Deng, L. Recent advances in development of magnetic garnet thin films for applications in spintronics and photonics. *Journal of Alloys and Compounds* **860,** 158235. ISSN: 0925-8388 (2021).

41. West, A. R. *Solid state chemistry and its applications* (John Wiley & Sons, 2014).

42. Stan, M., Lach, R., Łańcucki, Ł., Rutkowski, B. & Bućko, M. M. Reaction sintering of dense gadolinium-iron garnet (GdIG) material. *Journal of the European Ceramic Society* **41,** 5264–5268 (2021).

43. Zanatta, S. **andothers**. Mechanosynthesis of gadolinium iron garnet. *Journal of the American Ceramic Society* **88,** 3316–3321 (2005).

44. Ali, W. F. F. W., Othman, M., Ain, M. F., Abdullah, N. S. & Ahmad, Z. A. Studies on the formation of yttrium iron garnet (YIG) through stoichiometry modification prepared by conventional solid-state method. *Journal of the European Ceramic Society* **33,** 1317–1324 (2013).

45. Ashcroft, N. W., Mermin, N. D. **andothers**. *Solid state physics* 1976.

46. *Bragg'sLaw* http://hyperphysics.phy-astr.gsu.edu/hbase/quantum/bragg.html.

47. Young, R. *The rietveld method* (1993).

48. Rodriguez-Carvajal, J. *FULLPROF: a program for Rietveld refinement and pattern matching analysis* **in** *satellite meeting on powder diffraction of the XV congress of the IUCr* **127** (1990).

49. Nagatani, T., Saito, S., Sato, M. & Yamada, M. Development of an ultra high resolution scanning electron microscope by means of a field emission source and in-lens system. *Scanning Microscopy* **1,** 3 (1987).

50. Fleck, R. A. & Humbel, B. M. *Biological Field Emission Scanning Electron Microscopy, 2 Volume Set* (John Wiley & Sons, 2019).

51. Okano, Y. **in** *Compendium of Surface and Interface Analysis* 563–569 (Springer Singapore, Singapore, 2018). ISBN: 978-981-10-6156-1.

52. *Sputtering* http://www.semicore.com/what-is-sputtering.

53. *MagSputtering* https://www.adnano-tek.com/magnetron-sputtering-deposition-msd.html.

54. Binnig, G., Quate, C. F. & Gerber, C. Atomic Force Microscope. *Phys. Rev. Lett.* **56,** 930–933 (9 **march** 1986).

55. *AFM Theory* https://afm.oxinst.com/outreach/how-does-an-afm-microscope-work.

56. *FESEM* https://www.vcbio.science.ru.nl/public/pdf/feseminfoeng.pdf.

57. Sahu, N. & Panigrahi, S. Mathematical aspects of Rietveld refinement and crystal structure studies on PbTiO 3 ceramics. *Bulletin of Materials Science* **34,** 1495–1500 (2011).

58. Jiaqian, W., Jian, Y., Yulong, J. & Tai, Q. Effect of manganese addition on the microstructure and electromagnetic properties of YIG. *Journal of Rare Earths* **29,** 562–566 (2011).

59. Henderson, J. & White, R. Thermodynamic and magnetic properties of ytterbium iron garnet. *Physical Review* **123,** 1627 (1961).